



UNIVERSITY OF LEEDS

This is a repository copy of *Evolution of rimmed carbonate platform architecture controlled by sea-level change: Insights from the Lower-Middle Cambrian of the Northern Tarim Basin, China*.

White Rose Research Online URL for this paper:

<https://eprints.whiterose.ac.uk/223386/>

Version: Accepted Version

---

**Article:**

He, Q., Shi, K., Ma, Y. et al. (7 more authors) (2025) Evolution of rimmed carbonate platform architecture controlled by sea-level change: Insights from the Lower-Middle Cambrian of the Northern Tarim Basin, China. *Marine and Petroleum Geology*, 171. 107215. ISSN 0264-8172

<https://doi.org/10.1016/j.marpetgeo.2024.107215>

---

This is an author produced version of an article published in *Marine and Petroleum Geology*, made available under the terms of the Creative Commons Attribution License (CC-BY), which permits unrestricted use, distribution and reproduction in any medium, provided the original work is properly cited.

**Reuse**

This article is distributed under the terms of the Creative Commons Attribution (CC BY) licence. This licence allows you to distribute, remix, tweak, and build upon the work, even commercially, as long as you credit the authors for the original work. More information and the full terms of the licence here:

<https://creativecommons.org/licenses/>

**Takedown**

If you consider content in White Rose Research Online to be in breach of UK law, please notify us by emailing [eprints@whiterose.ac.uk](mailto:eprints@whiterose.ac.uk) including the URL of the record and the reason for the withdrawal request.



[eprints@whiterose.ac.uk](mailto:eprints@whiterose.ac.uk)  
<https://eprints.whiterose.ac.uk/>

1 **Evolution of rimmed carbonate platform architecture controlled**  
2 **by sea-level change: insights from the Lower-Middle Cambrian of**  
3 **the Northern Tarim Basin, China**

4 Qing He<sup>1</sup>, Kaibo Shi<sup>1\*</sup>, Yongsheng Ma<sup>1</sup>, Bo Liu<sup>1\*</sup>, Jun Han<sup>2</sup>, Jun Li<sup>1</sup>, Xiangyu Bai<sup>1</sup>, Chun Wu<sup>1</sup>,  
5 Adam D. McArthur<sup>3</sup> and Nigel P. Mountney<sup>3</sup>

6

7 <sup>1</sup>School of Earth and Space Sciences, Peking University, Beijing, 100871, China

8 <sup>2</sup>Northwest Oilfield Company, Sinopec, Urumqi, 830111, China

9 <sup>3</sup>Institute of Applied Geosciences, University of Leeds, Leeds, LS2 9JT, UK

10 **Abstract**

11 The sedimentary architecture of carbonate platforms is determined by distinct paleobiological,  
12 tectonics, climatic, oceanic and environmental conditions. During the Cambrian period, a rimmed  
13 carbonate platform system developed over an area of  $\sim 28 \times 10^4$  km<sup>2</sup> in the Tarim Basin. However,  
14 the evolution mechanism and its predominant controlling factors remain poorly understood. The  
15 investigation utilized integrated analysis of cores, thin sections, 3-D seismic, well logging and  
16 geochemical data to explain the sequence stratigraphic framework, depositional architecture and  
17 main controlling factors. Sixteen distinct microfacies (MF1–MF16) are identified based on thin-  
18 section analysis of the five lithofacies, which could be further grouped into fourteen microfacies  
19 associations (MA1-MA14). These fourteen microfacies associations respectively represent fourteen  
20 facies belts of the five facies of the shelf, outer ramp, middle ramp, platform margin and restricted  
21 platform. Microfacies and seismic characteristics have provided the basis for establishing a  
22 sequence-stratigraphic framework. Two regionally extensive second-order sequences (CS1-CS2)  
23 are developed in the Lower-Middle Cambrian succession; CS1 incorporates five third-order  
24 sequences (Sq1-Sq5); CS2 incorporates three third-order sequences (Sq6-Sq8). The lateral  
25 migration and vertical arrangement of depositional facies resulted in a unique depositional  
26 architecture. The overall carbonate platform architecture is interpreted from 3D seismic data,  
27 integrated with the depositional facies interpretations to document the evolution of the depositional  
28 setting over time from a broad shelf (Sq1-Sq2), to a distally steepening ramp (Sq3-Sq4), to a weakly  
29 rimmed platform (Sq5), and finally to a strongly rimmed platform (Sq6-Sq8). Relative sea-level  
30 (RSL) curves were reconstructed through an integrated analysis of Fischer plots from three wells.  
31 The determined RSL curve matches closely with reconstructed paleo-water depths indicated by the  
32 distribution of microfacies types. The inferred paleo-water depths changes comprise two long-term  
33 shallow–deep–shallow trends, upon which eight intermediate-term cycles are superimposed.  
34 Microfacies also have been applied to explain the evolution of the platform in response to RSL  
35 change and other environmental factors. A major transgression occurred in the lower parts of CS1.

36 Results demonstrate that RSL and paleo-water depth changes in the Lower-Middle Cambrian are  
37 consistent with known global sea-level changes indicated by geochemical elements. The  
38 architectural and sequence-stratigraphic evolution of the progradational rimmed carbonate platform  
39 was controlled principally by eustasy. This study is important due to the limited information on  
40 Cambrian rimmed platforms.

41

42 **Key words:** Cambrian, microfacies, sequence stratigraphy, platform architecture, sea-level change,  
43 Tarim Basin

## 44 1. Introduction

45 Carbonate platforms develop and grow principally in response to changes in biology, carbonate  
46 productivity, tectonics, climate, allochthonous sediment input, and eustasy (Heldt et al., 2010;  
47 Phelps et al., 2014; Pomar et al., 2015; Pomar et al., 2004; Scott et al., 1993; Yu et al., 2011). The  
48 margins of many rimmed carbonate platforms are sites of reef-shoal accumulation, and such stratal  
49 bodies form important reservoir units that host various resources of economic significance (Castro  
50 et al., 2008; Gao and Fan, 2015; Graziano, 2000; Santantonio et al., 2013; Zhu et al., 2015; Wang  
51 et al., 2024; Wang et al., 2025). The highly diverse carbonate factories and changes in  
52 accommodation space driven by sea-level rise and regional tectonics add significant complexity to  
53 seismic interpretation, sedimentological analysis, and hydrocarbon exploration (Markello et al.,  
54 2008; Wright and Burgess, 2005). Different types of carbonate factories have distinct carbonate  
55 sediment production rates, depth distributions, and grain sizes, which significantly impact the  
56 geometric morphology of carbonate platforms (Pomar and Hallock, 2008; Schlager, 2003). Sea-  
57 level fluctuations play a crucial role in determining spatiotemporal evolutionary processes and  
58 facies distributions within carbonate platforms (Wagner et al., 2004). However, in specific tectonic  
59 settings, such as where carbonate platforms develop rotational fault-blocks, the changes in  
60 accommodation space generated by tectonics can override the eustatic effect (Bosence et al., 1998).

61 After Ordovician, the rimmed carbonate platform margins were characterized by reefs built by  
62 corals and certain species of clams, which serve as barriers that drastically reduce wave energy (Xu  
63 et al., 2023). Prior to the Ordovician, the general absence of macroscopic reef-building organisms  
64 and the abundance of micro-organisms acted to limit the scale and extent of many platform-margin  
65 systems (Wood et al., 2019; Zhuravlev and Wood, 2018). Globally, few distinct rimmed carbonate  
66 platforms developed during the Ediacaran-Cambrian period. During the Cambrian, large-scale reef-  
67 shoals that apparently migrated continuously and rapidly under the influence of wave and tidal  
68 currents accumulated on carbonate platform margins in the Tarim Basin (Huang et al., 2020). The  
69 paleogeographic and spatiotemporal evolution of these Cambrian platform margins has been the  
70 focus of several studies in recent years. Importantly, the scheme for the stratigraphic subdivision in  
71 the platform margin remains uncertain due to the chaotic nature of the seismic reflections in this  
72 region. Gao and Fan (2015) and Huang et al. (2020) identified depositional evolutionary processes

73 within two sedimentary settings: ramp and rimmed platform. These authors delineated the zone of  
74 platform-margin development via interpretation of seismic reflection profiles. Zhang et al. (2021)  
75 identified the stages of evolution of the reef-shoal on the Cambrian platform margin and  
76 reconstructed the paleogeomorphology within the marginal zone. However, the main factors  
77 controlling the evolution of the Cambrian carbonate platforms of the Tarim Basin, and the drivers  
78 of the proliferation and widespread accumulation of platform-margin reef-shoals, remain unclear.

79 In this study, we utilise a subsurface dataset of 3D seismic, wireline well logs, core,  
80 petrographic and geochemical data to investigate the evolution process and main controlling factor  
81 of the Cambrian carbonate platforms of the Tarim Basin. The Lower-Middle Cambrian sequence  
82 stratigraphic framework and the evolutionary trends of the rimmed carbonate platform are  
83 established by detailed analysis of microfacies and their associations. An integrated analysis of  
84 Fischer plots obtained by continuous wavelet transformation, carbon and oxygen isotopes, and  
85 microfacies allows for the reconstruction and comparison of paleo-water depth and sea-level  
86 changes. Importantly, this study discusses the influences of paleocurrent directions, tectonic activity,  
87 global sea-level changes, and changes in other environmental controlling factors on the Cambrian  
88 rimmed platform evolution in the Tarim Basin. Results provide valuable insights into the processes  
89 acting upon and controlling Ediacaran-Cambrian rimmed carbonate platform development more  
90 generally.

## 91 **2. Geological setting**

92 The Tarim Basin is a sedimentary basin ( $56 \times 10^4 \text{ km}^2$ ) located in northwest China (Fig. 1a). It  
93 is bordered by the Kunlun-Altyn Mountains of the Tethys system to the south, and by the Tianshan  
94 Mountain of the Paleo-Asian system to the north (Fig. 1b; Lin et al., 2011). In the Neoproterozoic,  
95 the Tarim Basin was affected by extension due to the break-up of the Rodinia Supercontinent (Huang  
96 et al., 2005). During the Ediacaran-Cambrian transition period, the “Snowball Earth” event,  
97 characterized by extreme glaciation, impacted the climate and sedimentary processes in the Tarim  
98 Basin (Shang et al., 2020). During the Cambrian, “Cambrian explosion” occurred, known as a rapid  
99 diversification of life forms. This biological event had a significant impact on the marine  
100 environments, as the proliferation of life influenced the types of sediments being deposited (Servais  
101 et al., 2023). The Tarim Basin was located in a low-latitude zone near the equator that suggests a  
102 hot and arid climate for the region (He et al., 2016). The depositional paleogeomorphology of the  
103 basin was controlled by late Ediacaran tectonic activity (Ge et al., 2014; Li et al., 2013; Shi et al.,  
104 2018), and featured three uplifts: the Lunnan-Yaha Uplift, Keping-Wensu Uplift and southwestern  
105 Uplift; these were separated by two depressions developed between them (Zhu et al., 2019). The  
106 Early Cambrian syn-sedimentary structures in northern Tarim Basin mainly include syn-  
107 sedimentary faults (Gao et al., 2022; Guan et al., 2019; Yang et al., 2017). Hereafter, in response to  
108 gradual tectonic subsidence, the paleogeographic framework slowly changed, whereby a paleo-high  
109 developed in the west and a paleo-low developed in the east of the Tarim Basin (Fig. 2; Wei et al.,

110 2021). During the Phanerozoic, multiple episodes of tectonic activity and deformation associated  
111 with the Caledonian, Hercynian, Indosinian, and Himalayan orogenies transformed the Tarim Basin  
112 into a superposed complex basin with a Mesozoic–Cenozoic foreland cover overlying the earlier  
113 Paleozoic intracratonic basin fill (Jia, 1999). This study focuses on the Tabei Uplift in the northern  
114 Tarim Basin (Fig. 1b), which is situated at the periphery of the Lunnan-Yaha Uplift.

115 The Cambrian succession is characterized by several distinct carbonate sedimentary systems.  
116 Together, these record evidence of a transition from a shallow-water marine to a deeper basinal  
117 setting (Fig. 2 and Fig. 3). Taking the Lunnan-Gucheng platform margin zone as the line of  
118 demarcation (Cao et al., 2018; Ni et al., 2015; Yan et al., 2018), strata of Cambrian are divided into  
119 three major packages, each located in a distinct sub-region; each representing a different  
120 paleoenvironment in the Tarim Basin (Jiang et al., 2021b). The platform interior and the platform  
121 margin are located in the western part of the Tarim Basin, whereas the basinal region is located in  
122 the eastern Tarim Basin (Fig. 1b; Feng et al., 2006). The platform margin is the transitional region  
123 between the shallow-water platform and the deeper-water basin.

124 The Lower Cambrian succession comprises the Yuertusi, Xiaoerbulake and Wusonggeer  
125 Formations. The Yuertusi Formation is composed of organic-rich argillite (Chen et al., 2015a; Chen  
126 et al., 2015b). The Xiaoerbulake Formation is composed of micritic dolomite, microbial dolomite  
127 and dolo-grainstone in the western platform zone (Jiang et al., 2021b), whereas it is composed of  
128 micritic limestone and dolomitic limestone in the eastern platform zone, and contains argillite in the  
129 basin zone (Hu et al., 2019). The Wusonggeer Formation is composed of argillaceous dolomite,  
130 gypsum dolomite and evaporite in the western platform zone, whereas it is composed of microbial  
131 dolomite and dolo-grainstone in the eastern platform zone, and contains argillite and carbonaceous  
132 mudstone in the basin zone (Bai et al., 2019). The Middle Cambrian succession comprises the  
133 Shayilike and Awatage Formations, which are composed of deposits dolo-grainstone and microbial  
134 dolomite in the eastern platform zone, and of argillite in the basin zone (Gao and Fan, 2015).  
135 However, in the western platform zone, the Shayilike Formation is composed of micritic limestone,  
136 whereas Awatage Formation is dominantly composed of argillaceous dolomite and evaporate  
137 (Zhang et al., 2023).

### 138 **3. Data and methods**

139 The present study is based on data from five wells Y1, Y2, Y3, Y4 and Y5 penetrating or  
140 drilling the Lower-Middle Cambrian succession with thickness of 1123.5 m, 1034.5 m, 856 m  
141 1087.5 m and 884 m, respectively, and 3-D seismic dataset in the Tabei Uplift of the Tarim Basin.  
142 The well-logging data studied include natural gamma ray logs. Detailed observations and  
143 descriptions were made from 2749 thin sections of drill cutting from five wells (Y1, Y2, Y3, Y4 and  
144 Y5) and 40 thin sections of 222 cores with a cumulative length of 59.49 m from three wells (Y1, Y4  
145 and Y5). The thin sections of cuttings were sampled at one-meter (wells Y1 and Y4) and five-meter  
146 (wells Y2, Y3 and Y5) intervals.

147 The study of microfacies was based primarily on the analysis of cores and thin sections (Fig. 4  
148 and Fig. 5). The classification of microfacies was dependent on the identification of depositional  
149 and diagenetic fabric, grain type, biological allochem type, and matrix type in the thin sections  
150 (*sensu* Flügel, 2010). Based on Dunham's (1962) carbonate classification system, the abundance of  
151 argillaceous components, gypsum content and diverse types of grains and fossils were determined  
152 visually using a polarizing microscope. The proportions of individual microfacies types in the  
153 microfacies associations were depicted on stacked bar charts (Fig. 6 and Fig. 7). From this, four  
154 measures of relative abundance were defined: abundant (>50%), frequent (25–50%), less common  
155 (10–25%), and rare (<10%). By combining data studied herein with the research results of Wilson  
156 (1975) and Flügel (2010) on microfacies and microfacies associations, the characteristics of the  
157 depositional facies were analyzed and established.

158 The stratal stacking patterns of microfacies units and their associations thereof were  
159 determined and checked via calibration of well data and 3-D seismic profiles. These data were used  
160 to identify sequence boundaries and to establish a sequence-stratigraphic framework. Sequence  
161 stratigraphic interpretations were made to constrain the stacking patterns of depositional  
162 architectural units (Catuneanu et al., 2009). Fischer plots constructed from the 5 studied wells were  
163 drawn based on a recognition of high-frequency cycles via analysis of continuous wavelet transform  
164 of the gamma-ray logging data (cf. Yu et al., 2022). For the analysis of carbon and oxygen isotopes,  
165 the cutting samples were reacted with anhydrous phosphoric acid and the purified CO<sub>2</sub> was tested  
166 by a Thermo MAT-253 mass spectrometer at Beijing Research Institute of Uranium Geology.  
167 Microfacies, microfacies associations, Fischer plots, and carbon and oxygen isotopes were  
168 interpreted to reconstruct a history of paleo-water depth and relative sea-level changes (Geyman et  
169 al., 2021; Naderi-Khujin et al., 2020; Zadeh and Shafeii, 2021).

## 170 **4. Results**

### 171 **4.1. Microfacies characteristics and environment interpretation**

172 Based on observations and comprehensive analysis of thin sections, five lithofacies types  
173 (argillite, argillaceous carbonate, carbonate, gypsum carbonate and evaporite) can be divided into  
174 sixteen microfacies (MF1-MF16; Fig. 4 and Fig. 5), including argillite (MF1), argillaceous  
175 carbonate (MF2 and MF9), carbonate (MF3-MF8 and MF10-MF14), gypsum carbonate (MF15)  
176 and evaporite (MF16). Different microfacies were deposited under different hydrodynamic  
177 conditions and depositional environments. A summary of the identifying characteristics of each of  
178 these microfacies and their occurrence in microfacies associations is presented in Table 1.

### 179 **4.2. Microfacies associations characteristics and depositional facies**

180 To characterize the local depositional environments in more detail, the characteristics of  
181 combinations of microfacies that occur in vertical successions as microfacies associations have been

182 studied. Based on their relative abundance and order of vertical stacking, microfacies were assigned  
183 to 14 distinct microfacies associations (MA1-MA14), each of which is interpreted to record different  
184 depositional facies in the study area (Fig. 6 and Fig. 7). Vertical facies successions are commonly  
185 arranged into repeating meter-scale cycles; the internal facies composition and arrangement of these  
186 cycles is described in the sections that follow.

#### 187 **4.2.1. Shelf Facies Association (MA1-MA2)**

##### 188 4.2.1.1 MA1- Deep shelf

189 *Composition:* MA1 is characterized by the abundant presence of MF1 (A), the frequent  
190 presence of MF2 (F), the less common presence of MF3 (C), and the rare presence of MF4 (R; Fig.  
191 6a). MF1 is rich in black organic asphalt, containing siliceous spicules (Fig. 4a). The mud in MF2  
192 exhibits a zonal distribution (Fig. 4b). The meter-scale cycles formed by MA1 generally contain  
193 MF1 in their lower part, and MF2 in their upper part (Fig. 6b). MA1 is developed in the lower  
194 Yuertusi Formation, with a total thickness of ~25-35 m (Fig. 8). Vertically, MA1 commonly grades  
195 upward into MA2.

196 *Interpretation:* MA1 records deposition in a very low- to low-energy setting. The large amount  
197 of organic asphalt in the argillite indicates that these deposits accumulated in a reducing depositional  
198 environment (Jiang et al., 2021a; Zhou et al., 2015). Sponge spicules indicate 100-200m deep-water  
199 conditions (Beauchamp and Grasby, 2012; Wang et al., 2021). In addition, MA1 is widely  
200 distributed and changes rapidly longitudinally, likely indicating that it formed in response to rapid  
201 marine transgression (Lin et al., 2008). Collectively, these features suggest that MA1 was deposited  
202 in a deep shelf environment.

##### 203 4.2.1.2 MA2- Shallow shelf

204 *Composition:* MA2 is characterized by MF3 (A), MF6 (F), MF2 (R) and MF4 (R). Calcite and  
205 dolomite in MF6 are distributed in patches (Fig. 4h). Eighty per cent of the MF3 is present in the  
206 lower part of the meter-scale cycles formed by MA2 (Fig. 4c), and MF6 is developed in the upper  
207 part (Fig. 6c). MA2 occurs commonly in the Tabei Uplift, and is developed in the upper Yuertusi  
208 Formation, with a total thickness of ~15-35 m (Fig. 9).

209 *Interpretation:* The dominance of MF3 and MF6 in MA2 indicates accumulation in a low-  
210 energy depositional environment. The presence of MF6 reveals that the water depth was shallow  
211 (Montanez and Read, 1992; Noorian et al., 2022). In addition, the meter-scale cycles of MA2 overlie  
212 the deposits of MA1. Based on the superposition of microfacies associations, MA2 was deposited  
213 in a shallow-marine shelf environment.

#### 214 **4.2.2. Ramp Facies Association (MA3-MA7)**

##### 215 4.2.2.1 MA3- Outer ramp

216 *Composition:* MA3 is characterized by MF3 (A), MF4 (C), MF6 (C) and MF2 (R). In addition,  
217 vertically, MA3 normally overlays MA2. The bottom parts of the meter-scale cycles formed by  
218 MA3 are dominated by MF3, whereas the top is characterized by the development of MF4 (Fig. 6d).

219 MA3 occurs mainly in well Y4, and is developed in the lower Xiaerbulake Formation with a total  
220 thickness of ~50 m (Fig. 10).

221 *Interpretation:* the dominant occurrence of MF3 in MA3 indicates a low-energy depositional  
222 environment (Osleger, 1991). Less common MF4 and rare MF6 indicate a relatively deep  
223 environment. The small thickness of MA3 in the east and its restricted distribution in the study area  
224 indicate that the depositional environment was relatively deep and the sediment supply was low  
225 (Pomar et al., 2005). Collectively, these features suggest that MA3 was deposited in an outer ramp  
226 setting.

#### 227 4.2.2.2 MA4-Outer middle ramp

228 *Composition:* MA4 is characterized by MF4 (A), MF6 (F), MF3 (C) and MF5a (R). Part of  
229 MF6 was formed after the dolomitization of MF4, and most of MF3 has been subject to  
230 recrystallization with very fine calcite. Vertically, MA4 overlays MA3. The meter-scale cycles  
231 formed by MA4 generally contain MF3 at the bottom and MF4 (Fig. 5e) in the lower part of the  
232 cycle. The upper part of the cycle is characterized by MF6. MA4 is developed to the west of MA3  
233 and occurs mainly in wells Y1, Y2 and Y3 with a total thickness of ~150-370 m (Fig. 8 and Fig. 9).

234 *Interpretation:* MF4 indicates a low- to moderate-energy depositional environment (Tucker,  
235 1990). The proportion of MF4 and MF6 is more than 75% of the total in MA4, which is greater than  
236 their proportions in MA3 (20%; Fig. 6a). This indicates that MA4 was deposited in shallower water  
237 than MA3 and the sediments were more occasionally susceptible to current influence (Bosence et  
238 al., 2000). MA4 was likely deposited in the outer part of the middle ramp.

#### 239 4.2.2.3 MA5- Inner middle ramp

240 *Composition:* MA5 is characterized by MF6 (A), MF7 (F), MF4 (C), MF3 (R) and MF5 (R).  
241 Calcite in MF7 is dispersed within dolomite (Fig. 4i). Vertically, MA5 overlays MA4. The bottom  
242 of the meter-scale cycles formed by MA5 is dominated by MF4. The lower part contains MF6,  
243 whereas the upper part contains a large set of MF7 (Fig. 6f). MA5 occurs mainly in well Y1, and is  
244 developed in the middle-upper Xiaerbulake Formation (Fig. 8).

245 *Interpretation:* the dominance of MF6 and MF7 suggests that MA5 is developed in a low-  
246 energy depositional environment. The occurrence of MF7 indicates MA5 accumulated in a  
247 shallower-water setting than MA4. The observed features and relationships suggest that MA5 was  
248 deposited in the inner part of the middle ramp.

#### 249 4.2.2.4 MA6- Lagoon of middle ramp

250 *Composition:* MA6 is characterized by MF6 (A), MF9b (F), MF4 (F), MF7 (C), MF5 (C), and  
251 MF3 (R). Thin layers of MF5b (3-5 cm thick) are distributed in MA6. The bottommost parts of the  
252 meter-scale cycles formed by MA6 are dominated by MF6. The lower part contains MF4 and MF5  
253 (Fig. 4e and Fig. 4f), whereas the upper part contains a large set of MF7 and MF9 (Fig. 6g). MA6  
254 occurs mainly in well Y1 and is developed in the upper part of the Xiaerbulake Formation with a  
255 total thickness of ~120 m. Laterally, MA6 is developed to the west of MA7 (Fig. 8).

256 *Interpretation:* The occurrence of 70% of MF6 and MF9b in the MA6 indicates that the  
257 environment was low- to moderate energy and restricted, likely in a proximal middle ramp setting.



258 MF5b is developed in the strata with thin layers, revealing the intermittent occurrence of storms  
259 (Scholle and Ulmer-Scholle, 2003). MF5b indicates a shallow-water, high-energy environment  
260 (Flügel, 2010). The variety of microfacies present in this environment was likely due to a variable  
261 water energy regime. Collectively, these features suggest that MA6 was deposited in a lagoon of a  
262 middle ramp environment.

#### 263 4.2.2.5 MA7- Shoal of middle ramp

264 *Composition:* MA7 is characterized by MF5 (A), MF13 (F), MF7 (C) and MF6 (C). MF5 is  
265 composed of ooid and sand-sized intraclasts with partial dolomitization (Fig. 4g). MF13 preserves  
266 a residual phantom of its original structure (Fig. 5f). Vertically, MA7 overlies MA5. In the lower  
267 part of the meter-scale cycles formed by MA7, MF5a and MF5c are developed. MF13 is commonly  
268 observed in the upper part (Fig. 6h), which is mainly present in well Y2 and is developed to the east  
269 of MA6; typical thickness ~100 m (Fig. 9).

270 *Interpretation:* MF13 and MF5, with sparite cement, are interpreted to be typical sediments in  
271 shallow-water, medium-to-high-energy environments (Elrick and Read, 1991). Previous studies  
272 suggested that sea-floor topography (i.e., local relief) and sea level jointly act to control the location  
273 of high-energy shoals, whereby small changes in seabed topography might lead to conditions  
274 favorable for the development of shoals (Burchette and Wright, 1992). MA4 is considered to be a  
275 shoal deposit of the middle ramp environment.

### 276 4.2.3. Semi-restricted to restricted platform Facies Association (MA8-MA12)

#### 277 4.2.3.1 MA8- Muddy dolomite flat

278 *Composition:* MA8 is characterized by MF9 (A), MF8a (F), MF10 (C) and MF15 (R). The mud  
279 is mostly distributed in a lamellar form in MF8a (Fig. 4j). Vertically, MA5 overlays MA4. The  
280 meter-scale cycles formed by MA8 generally contain MF9 and MF8a in the lower part (Fig. 7b).  
281 MA8 occurs mainly in well Y1 and is developed in Wusonggeer and Awatage formations with a  
282 total thickness of ~40-60 m (Fig. 8).

283 *Interpretation:* MA8 is dominated by MF8a and MF9 and was deposited in a shallow-water  
284 and low-energy depositional environment (Lai et al., 2021; Longhitano et al., 2012). The laminated  
285 mud is interpreted as a tidal flat deposit in a restricted environment (Daidu et al., 2013). These  
286 features suggest that MA8 was deposited in the muddy dolomite flat area of a restricted platform.

#### 287 4.2.3.2 MA9- Dolomite flat

288 *Composition:* MA9 is characterized by MF8b (A), MF8a (F), MF10 (F) and MF8c (C). MF9a  
289 developed argillaceous laminae (Fig. 4k). Microcrystalline dolomite has semi-planar-s and planar-s  
290 crystal structure characteristics (Fig. 4l). Ten per cent of MF8c is developed in MA9 (Fig. 5a). Thirty  
291 per cent of MF8a is present in the lower part of the meter-scale cycles formed by MA9, and MF8b  
292 is developed in the upper part (Fig. 7c). MA9 occurs mainly in the Shayilike Formation (wells Y1  
293 and Y2; Fig. 8 and Fig. 9) and in the upper Awatage Formation (wells Y3, Y4 and Y5) with a thick  
294 thickness of ~40-80 m (Fig. 10).

295 *Interpretation:* MA9 is mainly composed of MF8a and MF8b, indicating that it was deposited  
296 in a low-energy and restricted environment (Hsu and Siegenth. C, 1969; Huang et al., 2009). The  
297 absence of mud and grains is suggestive of an open-water setting. Therefore, MA9 is considered as  
298 a dolomite flat deposit of semi-restricted platform environment.

#### 299 4.2.3.3 MA10- Gypsum-dolomite flat

300 *Composition:* MA10 is characterized by MF15 (A), MF9 (F), MF8b (C), MF11 (R) and MF16  
301 (R; Fig. 5l). The anhydrite nodules/agglomerates inside MF15 are isolated, or are connected laterally  
302 in the chicken-wire shape and filled in the water shrinkage joints produced by mud cracking (Fig.  
303 5k). Vertically, MA10 overlays MA9. The bottom of the meter-scale cycles formed by MA10 is  
304 dominated by MF9, whereas the top is characterized by the development of MF15 (Fig. 7d). MA10  
305 occurs mainly in wells Y1 and Y2; it is developed in Wusonggeer and Awatage formations (Fig. 8  
306 and Fig. 9).

307 *Interpretation:* MA10 is dominated by MF15 and MF9 deposited in a low-energy depositional  
308 environment. MF15 indicates a restricted evaporate tidal flat with high salinity (Zhong et al., 2022).  
309 The alternating occurrence of MF15 and MF9 reveals that the succession was influenced by daily  
310 changes of water level in the tidal flats (Diedrich, 2002; Herrmann et al., 2018; Yoshida et al., 2004).  
311 Collectively, these features suggest that MA10 was deposited in the gypsum-dolomite flat of a  
312 restricted platform.

#### 313 4.2.3.4 MA11- Inner shoal

314 *Composition:* MA11 is characterized by MF13 (A), MF12b (F), MF8a (F), MF8b (F) and MF10  
315 (R). MF12b has relatively poor sorting (Fig. 5e). The lower part of the meter-scale cycles formed  
316 by MA11 is dominated by MF8a and MF8b, whereas the upper part contains a large set of MF13  
317 intercalated with MF12b (Fig. 7e). MA11 occurs in Shayilike Formation (well Y2; Fig. 9) and upper  
318 Awatage Formation (wells Y4 and Y5; Fig. 10).

319 *Interpretation:* The dominant composition and intercalation of MF13, MF12b and MF8 in  
320 MA11 indicates rapid energy changes in a marine environment (Liu et al., 2020). MF12b reveals  
321 a high-energy environment without sufficient elutriation by water (Gao et al., 2015; He et al., 2017).  
322 The interior of MA8 and MA10 indicate a relatively open and moderate-energy environment.  
323 Based on the superposition of microfacies associations, MA7 was deposited in the inner shoal of  
324 semi-restricted platform.

#### 325 4.2.3.5 MA12- Inner mound

326 *Composition:* MA12 is characterized by MF14a (A), M8b (F), MF10 (C) and MF13 (C). The  
327 meter-scale cycles formed by MA12 generally contain M8b in the lower part of the cycle. The  
328 upper part is characterized by MF14a (Fig. 7f). MA12 occurs mainly in wells Y4 and Y5 in the  
329 upper Awatage Formation (Fig. 10).

330 *Interpretation:* The dominant composition of MF14a and MF8b in MA12 indicates deposition  
331 in a shallow-water, moderate- to high-energy depositional environment, similar to MA11. MA12  
332 occurs close to MA11 and the development of both MA12 and MA11 was likely controlled by  
333 locally elevated paleo-relief (Ren et al., 2023; Tan et al., 2022). MA12 is considered to represent

334 inner mound deposits of a semi-restricted platform.

#### 335 **4.2.4. Platform margin Facies Association (MA13-MA14)**

##### 336 4.2.4.1 MA13- Margin mound-shoal complex

337 *Composition:* MA13 is characterized by MF14a (A; Fig. 5g), MF14b (A; Fig. 5h), MF12 (F),  
338 MF13 (F), MF10 (C), MF11 (C; Fig. 5c) and MF14c (C; Fig. 5i). MF14b is present at the bottom of  
339 the meter-scale cycles formed by MA13. MF14a and MF13 can be observed in the lower part and  
340 MF14c and MF12 are observed in the upper part (Fig. 7g). MA13 occurs mainly in well Y2, Y3, Y4  
341 and Y5 in the eastern platform in the Wusonggeer Formation and Middle Cambrian (Fig. 9 and Fig.  
342 10).

343 *Interpretation:* MA13 is mainly developed in the platform margin; MF12, MF13, and MF14  
344 collectively indicate a shallow-water and moderate-to-high energy depositional environment. The  
345 interactive development characteristics of MF12 and MF14 reveals changes in water energy from  
346 moderate to high (James and Vonderborch, 1991; Rosenau et al., 2012). The large proportion of  
347 clasts of microbial origin indicates that MA13 is a mound-shoal complex deposit located on the  
348 platform margin.

##### 349 4.2.4.2 MA14- Margin shoal

350 *Composition:* MA14 is characterized by MF12a (A; Fig. 5e), MF12b (F), MF13 (F; Fig. 5f)  
351 and MF10 (C; Fig. 5b). MF12a is internally characterized by concentric growth structures (Fig. 5d).  
352 Vertically, MA14 overlays MA13, and in places alternates development with MA13. In the lower  
353 part of the meter-scale cycles formed by MA7, MF10 and MF13 is developed, whereas MF12a and  
354 MF12b tend to be present in the upper part (Fig. 7h). MA14 occurs mainly in wells Y2, Y3, Y4 and  
355 Y5 in the eastern part of the platform and is accompanied by MA13 (Fig. 9 and Fig. 10).

356 *Interpretation:* The presence of intergranular sprite cement in MF12 indicates that it was  
357 formed in a high-energy marine depositional environment (Elrick and Read, 1991). The high degree  
358 of particle sorting and rounding of grains in MF12 indicates formation after sufficient elutriation  
359 (Xi et al., 2017). The increase in dolo-grainstone content in MA14 indicates a depositional  
360 environment that was shallower than MA13. Therefore, MA14 is considered as a platform margin  
361 shoal deposit.

### 362 **4.3. Sequence stratigraphy**

363 The sequence stratigraphic framework for the Lower-Middle Cambrian succession in the study  
364 area has been established via integrated analyses of microfacies, stacking patterns of stratal  
365 packages composed of the various microfacies associations, and regional tracing of key reflections  
366 on the seismic data sets. The Lower-Middle Cambrian succession can be divided into two scales (cf.  
367 Catuneanu, 2019; Embry, 1993) of stratigraphic units: 2<sup>nd</sup>-order sequences within which 3<sup>rd</sup>-order  
368 sequences occur superimposed. In carbonate depositional systems, lowstand and falling stage  
369 systems tracts are poorly developed. Herein, an upward-deepening transgressive systems tract (TST)

370 and upward-shallowing regressive systems tract (RST) terminology has been used to subdivide the  
371 3<sup>rd</sup>-order sequences. Subaerial unconformities and maximum flooding surfaces (MFS) are identified;  
372 these are used to define sequence boundaries and systems tract boundaries, respectively (Catuneanu,  
373 2019; Catuneanu et al., 2006; Embry, 1993). Moreover, upward variations in stratal stacking patterns  
374 may also record transitions between systems tracts (Chen et al., 2001; Cloyd et al., 1990; Gil et al.,  
375 2006; Goldhammer et al., 1990; Osleger and Read, 1991).

376 In this study, the Lower-Middle Cambrian succession is divided into two 2<sup>nd</sup>-order sequences (CS1 and CS2; Fig.  
377 14 and

378 Fig. 15), both of which incorporate regional transgressive and regressive cycles. Sequences  
379 CS1 and CS2 are delineated by three 2<sup>nd</sup>-order megasequence boundaries (Msb): Msb1 (bottom of  
380 Lower Cambrian succession); Msb2 (top of Lower Cambrian succession); and Msb3 (top of Middle  
381 Cambrian succession).

382 Msb1 is represented by a large-scale regional unconformity in outcrops in the north-western  
383 Tarim Basin; this surface is associated with a distinctive karst breccia at the top of the Ediacaran  
384 (Gao et al., 2022; Zhao et al., 2011). In Well Y2, the interpreted depositional environment changes  
385 from tidal flat of an inner ramp below the surface (Chen et al., 2023), to deep shelf facies above the  
386 surface, with the microfacies changing from dolomite to argillite, respectively (Fig. 9). Karstic  
387 weathering and related evidence of exposure is not observed in cuttings or thin sections at the level  
388 of this boundary. However, the boundary is represented by a distinctive high-amplitude, continuous  
389 reflection in seismic profiles caused by the transition of lithotype from dolostone to argillite (Fig.  
390 12 and Fig. 13).

391 Msb2 is an unconformity generated by subaerial exposure in the north-western part of the  
392 Tarim Basin; collapse breccia is present atop the boundary (Ye et al., 2014). This boundary records  
393 a marked and abrupt change in microfacies, and thereby interpreted depositional environments  
394 below and above. In Well Y1, the depositional environment changed from an evaporate tidal flat  
395 below, to a dolomite flat environment above (Fig. 8), with microfacies changing from gypsum  
396 dolomite to microcrystalline dolomite, respectively. The boundary can be traced basin-wide in  
397 seismic profiles, with moderate-amplitude reflections caused by the transition of lithotype from  
398 gypsum dolomite to crystalline dolomite (Fig. 13a-b).

399 Msb3 records a major transgressive surface developed in response to regional sea-level rise. In  
400 Well Y1, the inferred depositional environment changed from evaporate tidal flat below, to a marine  
401 restricted platform environment above (Liu et al., 2016), with microfacies changing from gypsum  
402 dolomite and argillaceous dolomite to finely crystalline dolomite, respectively (Fig. 8). In the  
403 seismic cross-sections, this boundary is represented by a high-amplitude, continuous reflection (Fig.  
404 13a-b).

405 Within the major 2<sup>nd</sup>-order sequences, eight superimposed 3<sup>rd</sup>-order sequences (Sq1-Sq8) are  
406 recognized. Within these, six 3<sup>rd</sup>-order sequence boundaries (Sb1, Sb2, Sb3, Sb4, Sb5 and Sb6) are  
407 identified in the study area. The 3<sup>rd</sup>-order sequence boundaries record changes in depositional  
408 environments below and above as a result of sea-level fall and subsequent rise. The 2<sup>nd</sup>-order

409 sequence CS1 incorporates five nested 3<sup>rd</sup>-order sequences (Sq1, Sq2, Sq3, Sq4 and Sq5; Fig. 8-  
410 Fig. 10). The 2<sup>nd</sup>-order sequence CS2 incorporates three nested 3<sup>rd</sup>-order sequences (Sq6, Sq7 and  
411 Sq8; Fig. 8-Fig. 10).

## 412 **4.4. Seismic facies and stratigraphic units**

### 413 **4.4.1. Seismic facies interpretation**

414 In the 3D seismic volume of the carbonate platform in the Tarim Basin, eight seismic facies  
415 types (SMF1-SMF8) are identified based on different seismic reflection characteristics (internal  
416 reflection structure, continuity, amplitude and frequency) and external structure (Fig. 11).

### 417 **4.4.2. Seismic stratigraphic units and depositional architecture**

418 The Lower-Middle Cambrian strata are very thick (1000-1200 m) in the Tabei Uplift of the Tarim Basin. The  
419 evolution and distribution of depositional facies zones and their vertical and lateral variability (Yu et al., 2022; Zhang  
420 et al., 2015) remain unclear. Through the analysis of seismic reflection character, in combination with well-log data,  
421 cuttings and thin-section data from across the study area from the Tabei Uplift to the Manjiaer Depression, six  
422 stratigraphic units are identified in the studied Cambrian succession (Fig. 12 and Fig. 13). The spatiotemporal  
423 development of depositional facies under the isochronous framework in the Lower-Middle Cambrian has been  
424 mapped (Fig. 14 and

425 Fig. 15). Eight sequence boundaries, including three megasequence boundaries associated with  
426 the two 2<sup>nd</sup>-order sequences are identified in seismic profiles of the Lower-Middle Cambrian (Fig.  
427 13a). Six carbonate progradational sediment bodies can be identified in the seismic profiles.  
428 Progradational bodies Pb1 and Pb2 are developed in Sq4 and Sq5, respectively. Progradational body  
429 Pb3 is developed in the TST of Sq6. Progradational bodies Pb4, Pb5 and Pb6 are developed in the  
430 HSTs of Sq6, Sq7 and Sq8, respectively. Progradational bodies Pb3-Pb6 of the Middle Cambrian  
431 are more aggradational and more progradational than Pb1-Pb2 of the Lower Cambrian.

432 Seismic Line 1 passes through wells Y1, Y2, and Y4 in the Tabei area, and extends northeast  
433 from the Tabei Uplift to the northern part of the Manjiaer depression (Fig. 1b). The two-way travel  
434 time (TWTT) of the Cambrian sedimentary succession near the Aman Slope in the west is from  
435 about 4.35s to about 5.05s, which is similar to the TWTT of 3.85s to 4.45s for that in the eastern  
436 Tabei Uplift. However, the TWTT of the Xiaoerbulake Formation decreases sharply to the east of  
437 Well Y3. The TWTT of the Middle Cambrian succession increases significantly to the east of Well  
438 Y3 and decreases sharply into the Manjiaer depression (Fig. 12).

439 Seismic Line 2 passes through wells Y1 and Y5, and extends eastward from the Tabei Uplift  
440 to the northern part of the Manjiaer depression (Fig. 1b). The thickness of Xiaoerbulake Formation  
441 decreases sharply from a maximum in well Y1 (TWTT from 4.82s to 5.05s) eastwards (Fig. 13a).

#### 442 **4.4.2.1 Second-order sequence CS1**

443 *Seismic stratigraphic units:* The total thickness of the 2<sup>nd</sup>-order sequence CS1 in the west of  
444 the Tabei Uplift is greater than that in the east (Fig. 13). The 2<sup>nd</sup>-order sequence CS1 can be divided

445 into four parts, corresponding to 3<sup>rd</sup>-order sequence- Sq1, Sq2, Sq3, Sq4 and Sq5. The lower part of  
446 CS1 (Sq1-Sq2) contains parallel, high-amplitude, continuous seismic reflections (SMF3) and is  
447 crossed by several wells. The middle two parts (Sq3 and Sq4) change from subparallel-parallel,  
448 moderate- to high-amplitude, moderately to highly continuous reflections (SMF1 and SMF2) in the  
449 west, to parallel, high-amplitude, continuous seismic reflections (SMF1) in the east. It crossed by  
450 wells Y1 and Y4, respectively. The upper part (Sq5) is characterized by subparallel, moderate  
451 amplitude, and moderate-high continuous reflections (SMF4 and SMF5) in the west. It is crossed  
452 by wells Y1 and Y2. The central and eastern parts are composed of mounded, chaotic, low  
453 continuous reflection and subparallel-moderate continuous reflections (SMF7), which transform  
454 eastward to parallel, high-amplitude, continuous seismic reflections (SMF8) (Fig. 13b).

455 *Depositional architecture:* In Sq1-Sq2, there was little variation in the lateral distribution of  
456 depositional facies. Vertically, Sq1 resulted in the accumulation of deep shelf facies (MA1) and is  
457 mainly composed of MF1 and MF2. The following Sq2 resulted in the accumulation of shallow  
458 shelf facies (MA2) and consisted mainly of MF3 and MF6. In Sq3, wells Y1, Y2 and Y3 in the west  
459 were located in the outer part of the middle ramp (MA4), consisting of MF4 and MF6. Horizontally,  
460 well Y4 in the east was located in the outer ramp (MA3), containing MF3. In Sq4, the depositional  
461 environment of the succession representing TST4 observed in each well was similar to that of TST3  
462 in Sq3, while calcite content in Sq4 is reduced. The depositional environment in RST4 induced a  
463 vertical change from an outer middle ramp (MA4) setting to an inner middle ramp (MA5) and  
464 lagoon (MA6) setting. The MA5-MA6 is mainly composed of MF6-MF7. Well Y2 recorded shoal  
465 deposits (MA7) of a middle ramp setting, consisting of MF5 and MF13. In Sq5, the preserved  
466 thickness is greater in the east than in the west. In TST5, well Y2 was represented by mound-shoal  
467 complex (MA13) facies, containing MF14a and MF11 above the uppermost deposits of earlier RST4.  
468 In RST5, wells Y1 and Y2 recorded gypsum dolomite flat (MA9) and dolomite flat (MA8) deposits  
469 composed of MF8, MF9 and Mf15. Laterally, wells Y3 and Y4 began to develop platform margin  
470 shoal (MA14) deposits, consisting of MF10 and MF13. Generally, Sq5 preserved accumulations of  
471 two stages of platform-margin mound-shoal complexes (MA13) and one stage of platform margin  
472 shoal (MA14) deposit (Fig. 13c and Fig. 14).

#### 473 4.4.2.2 Second-order sequence CS2

474 *Seismic stratigraphic units:* The thickness of CS2 increases sharply from well Y1 to well Y5  
475 (Fig. 13a). Multiple progradational bodies, each with internal chaotic reflections, are identified in  
476 the platform margin (SMF6, SMF7) and crossed by wells Y4 and Y5. Subparallel, moderate  
477 amplitude, moderate-high continuous seismic reflections (seismic facies SMF4) are observed in the  
478 western platform. In addition, the deposits developed inside the platform margin shoals are  
479 characterized by subparallel-parallel, high amplitude, moderate-high continuous seismic reflection  
480 (SMF5; Fig. 13b).

481 *Depositional architecture:* In TST6 of Sq6, the depositional environment recorded in wells Y1  
482 and Y2 changed from the gypsum dolomite flat (MA10) to dolomite flats (MA9), consisting of MF8  
483 at the bottom and MF13 at the top. Laterally, wells Y3 and Y4 recorded development of a platform

484 margin shoal (MA14). While well Y3 consisted of high-energy MF12, well Y4 developed low-  
485 to moderate-energy MF13 (Fig. 10). In RST6, the depositional environment recorded in wells Y1  
486 and Y2 was gypsum-dolomite flat (MA10) composed of MF9 and MF15, whereas well Y3 changed  
487 to dolomite flat (MA11). Wells Y4 and Y5 recorded a mound-shoal complex (MA13) and platform  
488 margin shoal (MA14), consisting of MF14a, MF14b, MF12b and MF10, MF12a respectively. In  
489 TST7 of Sq7, wells Y1 and Y2 recorded gypsum-dolomite flat (MA10) and muddy dolomite flat  
490 (MA8), containing MF15 and MF9 respectively. Laterally, wells Y3 and Y4 recorded dolomite flat  
491 (MA9), and well Y5 recorded a transformation from a platform margin shoal (MA14) into a mound-  
492 shoal complex (MA13) composed of MF14a. In RST7, wells Y1 and Y2 recorded gypsum dolomite  
493 flat (MA10), consisting of MF9 and MF15. Laterally, wells Y3 and Y4 recorded dolomite flat (MA9)  
494 and intra-platform shoal (MA11), containing MF8 and MF13 respectively. Well Y5 recorded  
495 platform margin shoal (MA14) and mound-shoal complex (MA13). In TST8 of Sq8, the  
496 depositional environments recorded by successions in wells Y1, Y2 and Y3 remained similar. Well  
497 Y4 changed from an inner shoal (MA11) to an inner mound (MA12) composed of MF14a. Laterally,  
498 well Y5 recorded a change from a platform margin mound-shoal complex (MA14) to a dolomite  
499 flat (MA9) composed of MF8. In RST8, wells Y4 and Y5 recorded intercalated dolomite flat (MA9),  
500 inner shoal (MA11) and inner mound (MA12) deposits. Compared with Sq7, content of MF8 in Sq8  
501 is increased. Generally, the platform margin zone developed four stages of mound-shoal complexes  
502 (MA13) and five stages of shoals (MA14) deposits (Fig. 13c and  
503 Fig. 15).

## 504 **4.5. Fischer plots and isotopes**

### 505 **4.5.1 Fischer plots**

506 The Fischer plot was first proposed for the study of sea-level changes in cyclically arranged  
507 tidal-flat carbonate deposits (Fig. 16a). It was applied to explain the vertical stacking patterns of  
508 carbonate deposits and changes in accommodation with relative sea-level (Fischer, 1964). Previous  
509 studies have modified the original plotting method (Fig. 16b). However, the technique is not  
510 applicable in all conditions (Sadler et al., 1993). It is, however, suitable in cases where a shallow-  
511 water depositional environment has accumulated in response to accommodation generated via a  
512 steady rate of subsidence. Thick cycles generally record a long-term increase in accommodation  
513 space, whereby rapid relative sea-level rise was ongoing and uninterrupted. In contrast, thin cycles  
514 generally record a long-term decrease in accommodation, potentially caused by slow relative sea-  
515 level rise (cf. Goldhammer et al., 1990; Goldhammer et al., 1993). Therefore, the results of the  
516 Fischer-plot analysis can indicate change rate in relative sea-level.

517 The deposit cycles correlate with the scale factor of the Morlet wavelet function during the  
518 continuous wavelet transform, which can be used to analyze frequency characteristics of signals  
519 (Meyers et al., 1993). Generally, the recorded GR signals without uranium have a good response  
520 relationship to the identified microfacies (Fig. 8-Fig. 10). After performing continuous Morlet  
521 wavelet transform analysis on GR logging data, the wavelet coefficient curve which has notable  
522 cyclic properties can be obtained (Hu et al., 2018; Prokoph and Agterberg, 2000). Long-term surface

523 exposure may result in missing records of high-frequency sea-level fluctuations in coastal areas  
524 (Goldhammer et al., 1990). However, through the observation of thin sections in the study area, no  
525 obvious candidate long-term exposure surfaces (Colombié and Strasser, 2005; Osleger and Read,  
526 1991; Overstreet et al., 2003) were found in the interior of CS1 and CS2. By tracking specific points  
527 in the wavelet coefficient curves, the short-term periodic deposit cycles can be obtained. Based on  
528 the identified short-term high-frequency cycles, Fischer plots relating to data recovered from five  
529 wells are constructed (Fig. 8-Fig. 10 and 15; Guo et al., 2018a; Guo et al., 2018b; Wang et al., 2022;  
530 Yu et al., 2022).

531 The preserved depositional thickness of Sq1-Sq2 varies from 39 to 79.5 meters and the high-  
532 frequency cycles therein are on average only 0.5 meters thick (Fig. 8-Fig. 10). As such, these cycles  
533 are too thin to enable construction of a meaningful Fischer plot and to conduct continuous wavelet  
534 transform analysis. Therefore, analysis has been confined to the short-period, high-frequency cycles  
535 of Sq3-Sq5 in the Lower Cambrian (thickness max = 10.0 m; mean = 9.7 m; Min = 5.8 m), and to  
536 Sq6-Sq8 in the Middle Cambrian (thickness max = 14.2 m; mean = 9.5 m; min = 6.5 m). These  
537 high-frequency cycles correspond to the meter-scale cycles commonly about 10 m thick. Overall,  
538 well Y1 has the largest number of high-frequency cycles, well Y5 well has the least number of  
539 cycles, and well Y4 has the highest average thickness of cycles in Sq3-Sq8 (Table 2). Fischer plots  
540 have been constructed for these intervals, and six cycles can be identified on the cumulative  
541 deviation of average thickness in Sq3-Sq8 (Fig. 8-Fig. 10 and Fig. 16).

#### 542 **4.5.2 Carbon and oxygen isotopes**

543 Previous studies have shown that the carbon isotope composition of marine carbonate rocks  
544 has a strong correlation with the production and burial of organic carbon (Stephens and Sumner,  
545 2003). The generation and rapid burial of a large amount of organic carbon during major the  
546 episodes of global transgression period led to a decrease in  $^{12}\text{C}$  and a relative increase in  $^{13}\text{C}$  in  
547 seawater, resulting in a positive drift of  $\delta^{13}\text{C}$  in marine carbonate rocks (Tissot, 1979). In contrast,  
548 the exposure of the continental shelf during episodes of major global regression will lead to the  
549 oxidation of a large amount of organic carbon, which will lead to cause an increase in  $^{12}\text{C}$  and a  
550 relative decrease in  $^{13}\text{C}$  in seawater, resulting in a relative decrease in  $\delta^{13}\text{C}$  in marine carbonate rocks  
551 (Tissot, 1979). There is a negative correlation between  $\delta^{13}\text{C}$  in carbonate rocks and global sea-level  
552 changes (Shembilu and Azmy, 2021), e.g. global sea level rise would be accompanied by a positive  
553 drift in  $\delta^{13}\text{C}$ . The C and O isotopes are analyzed in the wells Y1, Y2 and Y4, and eight cycles can  
554 be identified based on the C isotopes changes (Fig. 8-10).

555 In well Y1, the depth of Sq1-Sq2 ranges from 8781.5-8744 m, and  $\delta^{13}\text{C}$  remained at a low  
556 value (Fig. 8). At the depth of 8744-8702 m,  $\delta^{13}\text{C}$  began to drift positively from -1.9‰ to -0.2‰  
557 (Fig. 8). In Sq3-Sq4, the thickness of most high-frequency cycles in the rising limb of the Fischer  
558 curve is greater than the average cycle thickness, and the corresponding  $\delta^{13}\text{C}$  was drift to more  
559 positive values about 1.2‰ (Fig. 8). In the descending limb of the Fischer curve, the thin high-



560 frequency cycles reflect a long-term decrease in accommodation space, and  $\delta^{13}\text{C}$  began to drift  
561 negatively from 0.7‰ to -0.4‰ in the uppermost part of Sq4 (Fig. 8). In Sq5, from base to top,  $\delta^{13}\text{C}$   
562 first drifts negatively, and then drifted positively from -0.8‰ to 0.7‰. In Sq6-Sq8, the rising limb  
563 of the Fischer curve corresponds to a positive drift of  $\delta^{13}\text{C}$ , whereas the descending limb of the  
564 Fischer curve corresponds to a negative drifting of  $\delta^{13}\text{C}$  (Fig. 8).

565 In well Y2, the variation of  $\delta^{13}\text{C}$  is similar to well Y1 in the Sq1-Sq2. In Sq3-Sq4, the rising  
566 limb of the Fischer curve is associated with the sudden positive drift of  $\delta^{13}\text{C}$  from -1.2‰ to 0.84‰  
567 (Fig. 9). The upper part of the descending limb of the Fischer curve in the Sq4 sequence corresponds  
568 to a gradual negative drift from 0.46‰ to -0.75‰ and small-amplitude fluctuations of  $\delta^{13}\text{C}$  (Fig. 9).  
569 In Sq5-Sq6, a large negative drift of  $\delta^{13}\text{C}$  changed from 1.29‰ to -0.06‰ is evident (Fig. 9). In  
570 Sq7-Sq8, the characteristics of the Fischer curve is similar to those observed in Y1 well, with both  
571 positive and negative drift in carbon isotope values (Fig. 9).

572 In well Y4,  $\delta^{13}\text{C}$  remained at a low value about -2.5‰ in Sq1-Sq2. In Sq3-Sq4, the thickness  
573 of Sq3-Sq4 is thin, and the rising limb of the Fischer curve corresponds to a gradual positive drift  
574 of  $\delta^{13}\text{C}$  from -1.1‰ to 0.6‰, whereas the descending limb of the Fischer curve is associated with a  
575 significant negative drift of  $\delta^{13}\text{C}$  from 0.6‰ to -0.3‰ (Fig. 10). In the rising limb of the Fischer  
576 curve in Sq5,  $\delta^{13}\text{C}$  experienced fluctuations but an overall positive drift from -0.4‰ to 0.8‰, while  
577 the descending limb of the Fischer curve is associated with a gradual negative drift from 0.8‰ to -  
578 0.1‰ (Fig. 10). In Sq6-Sq8, the rising and descending limb of the Fischer curve corresponds to a  
579 gradual positive and negative drift of  $\delta^{13}\text{C}$  respectively, while the rising and descending limb of the  
580 Fischer curve in Sq8 is associated with a sudden positive drift of  $\delta^{13}\text{C}$  from 0.7‰ to 2‰ (Fig. 10).

## 581 **5. Discussion**

### 582 **5.1. Sea-level changes**

583 The paleo-water depth and RSL changes indicated by the microfacies and Fischer plot can be  
584 divided into eight cycles of sea-level rise and fall, consistent with global sea-level changes  
585 represented by the carbon isotopes (Fig. 8-10). For each of the eight cycles, reconstructed paleo-  
586 water depth changed from shallow, to deep, and back to shallow. The eight moderate-term sea-level  
587 cycles correspond to the 3<sup>rd</sup>-order sequences (Sq1-Sq8) and to the sequence units identified in the  
588 seismic sections (Fig. 13). The eight cycles of sea-level rise and fall can be divided into two overall  
589 long-term sea-level cycles that correspond to the 2<sup>nd</sup>-order sequences (CS1-CS2). The rising limbs  
590 of Fischer curves and the positive carbon isotope drifts correspond to the transgressive system tracts  
591 of the 3<sup>rd</sup>-order sequences. The descending limbs of Fischer curves and negative drifts correspond  
592 to the regressive system tracts.

593 During the CS1, the overall sea-level was high, and the RSL rose rapidly at first with the MFS  
594 present in Sq1 (Fig. 8-10). As RSL rapidly rose to the MFS, the microfacies were mostly dominated  
595 by MF1 and MF2 in Sq1-Sq2, indicating a deep-water environment. Then the RSL occurred a slow

596 rise and regression in Sq3-Sq4, the paleo-water depth began to fall continuously, resulting in the  
597 disappearance of MF1 and the increase of MF5, MF7 and MF8 content. The depositional  
598 environment transformed from deep shelf to shallow ramp. Along with the RSL experienced  
599 regression in Sq5, the paleo-water depth reached the lowest, resulting in the appearance of MF13-  
600 MF15. The depositional environment is transformed into restricted platform and platform margin.  
601 During the CS2, the overall sea-level rose slowly; the MFS is present in Sq5 (Fig. 8-10). As RSL  
602 experienced a rapid and low-amplitude rise in Sq6, the paleo-water depth was deeper than Sq5,  
603 resulting in the short-term disappearance of MF15 and large-scale development of MF8, MF12 and  
604 MF13. The depositional environment became semi-restricted. Then the RSL occurred regression,  
605 the paleo-water depth began high-amplitude fall, resulting in the increase of MF15 content in the  
606 west and MF12-MF14 in the east. The restricted platform expanded broadly, and platform edge  
607 migrated eastward greatly. Overall, the RSL and paleo-water depth changes plays an important role  
608 in basin filling and sedimentary evolution.

## 609 **5.2. Main factors controlling the evolution of carbonate platform**

610 During the Cambrian, the Tarim Basin experienced an arid climate (Zhang et al., 2023). The  
611 basin was situated at a paleolatitude of between 30° north and south of the equator (Bai et al., 2017;  
612 Hoffman and Li, 2009). The water was warm and clear (cf. Schlager, 2003). These factors enabled  
613 the development of a major tropical shallow-water carbonate factory (Schlager, 2003). The  
614 interpreted paleo-wind direction changed from south-west to south-southwest in the Cambrian (Hu  
615 et al., 2023). The windward side had relatively high energy and developed microbial rocks (Berg  
616 and Pace, 2017; Michel et al., 2018), which were conducive to the formation of the rimmed platform.  
617 The high-angle of slope caused the carbonate deposits to accumulate in response to transport by  
618 waves, and enabled the formation of large-scale platform-margin mounds and shoals. Macro-reef  
619 building biological populations did not develop in the Cambrian, and microorganisms dominated  
620 by cyanobacteria played a leading role in the deposition and formation of carbonate rocks at the  
621 platform margin (Flügel, 2010; Pratt, 2009; Song et al., 2012). Moreover, water depth,  
622 hydrodynamic conditions and sediment types determined by RSL (relative sea-level) changes,  
623 controlled the morphology, internal structure and growth of the platform (Pomar, 2001). When water  
624 depth is below 60 m, microorganisms will probably multiply and are enabled to maintain high  
625 productivity (cf. Pomar and Haq, 2016), especially in the shallow and high-energy platform margin.

626 Paleo-water depth changes are controlled by regional tectonics, deposition rate and global sea-  
627 level changes (Vail, 1991). Deposition rate is relatively constant over the time of 3<sup>rd</sup>-order sequence  
628 and can be considered as a constant (Zhao, 2015). The biostratigraphy indicates that the Lower-  
629 Middle Cambrian was deposited in the Terreneuvian, Series 2 and Miaolingian (Chen et al., 2020).  
630 Comparison of the reconstructed paleo-water depth changes reported in this study with the global  
631 sea level curve (Haq and Schutter, 2008) and carbon isotopes curve, reveals that both contain six  
632 notable cycles of sea-level rise and fall – Sq3-Sq8 of this study (Fig. 17). This indicates that paleo-  
633 water depth changes reported here were consistent with models of global sea-level change. As such,  
634 global sea-level change was considered to be the main factor that controlled the structure and  
635 sedimentary evolution of the carbonate platform across this subsiding or passive margin that was  
636 subject to a relatively constant rate of basin subsidence (Bosence, 2005).

637 Overall, the development of the carbonate ramp in the Early Cambrian is attributed to the  
638 increase in carbonate production in the deep aphotic zone caused by the sea level decline (Huang et  
639 al., 2022). Whereas, the distal steepening feature in the eastern ramp is caused by the appearance of  
640 progradational bodies and the difference in subsidence rate between the Manjiaer Depression and  
641 the study area (Li et al., 2012). High-frequency sea level fluctuations will cause deposit to disperse  
642 and accumulated under deep water flat ramp, preventing forming high angle differential  
643 paleogeography (Williams et al., 2011). In the late Early Cambrian, as the sea level fall, the  
644 accommodation space decreased and the progradational bodies developed in the ramp setting. The  
645 progradational bodies continued to prograde from west to east and the difference in subsidence rate  
646 increased, resulting in a gradual increase in the angle of the ramp break. Due to the sea-level  
647 declined to the lowest value and its fluctuation range was small, making carbonate easy to deposit  
648 in situ (Williams et al., 2011). Affected by seawater waves and monsoons from the southwest to the  
649 west, the accumulation of moderate- to high-energy deposit increased the thickness and angle of the  
650 break, eventually forming a poorly rimmed carbonate platform.

651 In the Middle Cambrian, with the low-amplitude sea-level rise, the poorly rimmed carbonate  
652 platform margin has a greater production rate and continues to thicken to catch up with sea-level  
653 changes, causing a large amount of granular and microbial carbonate deposit. As deposits continued  
654 to accumulate, the paleogeography of the platform margin became higher, the slope angle became  
655 larger and the poorly rimmed carbonate platform transformed into a strongly rimmed carbonate  
656 platform. In addition, the obstruction of the platform margin and arid paleoclimate made the  
657 environment of intra-platform more restricted and the salinity of paleo-water increase. Since the  
658 high-salinity water environment is not conducive to the growth of microorganisms, microorganisms  
659 will accumulate at the platform margin near the open sea. Therefore, the platform margin has a  
660 higher carbonate production, making it more rimmed. As the accommodation space decrease caused  
661 by the continuous decline of sea-level, the platform margin prograde towards the basin, eventually  
662 forming a large-scale carbonate platform margin zone.

### 663 **5.3. Platform development and evolution pattern**

664 Since carbonate microfacies and platform types show great differences in time and space,  
665 establishing controls on depositional evolution is important (Gu et al., 2009; Pomar and Hallock,  
666 2008). Previous studies have suggested that platform margin reef deposits could be observed, and  
667 weekly rimmed carbonate platforms developed in the late Early Cambrian in the Northern Tarim  
668 Basin (Gao and Fan, 2015; Pomar, 2001; Tucker, 1990; Wei et al., 2021).

669 The characteristics of depositional facies and sea-level changes indicate changes from  
670 relatively deep to shallow paleo-water, humid to arid climate, and open to restricted environmental  
671 settings. Based on the spatial and temporal distribution of depositional facies, the Lower-Middle  
672 Cambrian successions of Northern Tarim Basin are divided into four depositional types: broad shelf  
673 (Sq1-Sq2), distal steepening ramp (Sq3-Sq4), weekly rimmed platform (Sq5), and strongly rimmed  
674 platform (Sq6-Sq8). This study identifies platform types similar to those identified previously  
675 (Burchette and Wright, 1992; Tucker, 1990; Wilson, 1975) and builds upon these to explain the  
676 occurrence of depositional patterns (Fig. 18). The position of the identified depositional  
677 environments within the overall platform settings can be evaluated by analyzing the microfacies

678 associations, paleo depositional profiles, and vertical and horizontal facies distribution (Noorian et  
679 al., 2021).

680 In the Lower Cambrian (Sq1-Sq5), the Tarim Basin was in a stable extensional tectonic  
681 background in the Early Caledonian (Liu et al., 2022). During Sq1-Sq2 period, along with  
682 substantial and rapid relative sea-level rise, broad deep shelf deposit developed, accompanied by  
683 syn-sedimentary faults and related siliceous hydrothermal activities (Fig. 18a). During Sq3-Sq4,  
684 regression occurred in RST3 (3) of Sq3 (3), with an increase in carbonate production in the deep  
685 aphotic zone and depositional pattern changing to the distal steepening ramp (Fig. 18b; Williams  
686 et al., 2011; Huang et al., 2022). The distal steepening was caused by different subsidence rate  
687 between the Manjiaer Depression and this study area (Li et al., 2012). RSL fluctuations caused  
688 sediments to disperse and are difficult to form under regional high paleogeography, such as in deep  
689 ramps (Williams et al., 2011). During Sq5 period, regression reached maximum extent in CS1 and  
690 the accumulation of moderate- to high-energy mound and shoal deposits developed along the slope  
691 (Gao and Fan, 2015; He et al., 2017), forming a weekly rimmed carbonate platform. Semi-restricted  
692 platform developed due to the blocking effect of margin mounds and shoal deposits (Fig. 18c).

693 In the Middle Cambrian (Sq6-Sq8), the Tarim Basin was dominated by strongly rimmed  
694 platform deposits. During TST5 of Sq6, a short-term period of rapid sea-level rise ensued; in  
695 response, the depositional environment in the western platform changed into the restricted-open  
696 platform. Due to the high carbonate production, deposits continued to thicken to catch up with  
697 relative sea-level changes in the platform margin (Huang et al., 2022), and a strongly rimmed  
698 carbonate platform developed (Fig. 19a). During RST5 to RST7, a long-term period of slow relative  
699 sea-level rise ensured and accommodation gradually decreased in response to ongoing  
700 sedimentation, the platform margin continued to prograde towards the basin, forming the large-scale  
701 platform margin zone. Due to the barrier of platform margin and the arid paleo-climate, salinity of  
702 paleo-water increased in the western platform which evolved into a restricted platform (Fig. 19b).

## 703 **6. Conclusions**

704 Based on the depositional facies, the sequence architecture and relative sea-level changes using  
705 well and core data for petrographic observations, geochemical data analyses, Fischer curves  
706 construction and integration with 3D seismic interpretation of the Lower-Middle Cambrian in the  
707 Tabei Uplift of the Tarim Basin, the following conclusions can be drawn.

708 1. From analysis of sixteen microfacies (MF1–MF16) and fourteen microfacies associations  
709 (MA1-MA14), fourteen depositional facies are recognized in the Lower-Middle Cambrian in the  
710 Northern Tarim Basin: deep and shallow shelf, outer ramp, inner middle ramp, outer middle ramp,  
711 lagoon and shoal of middle ramp, muddy dolomite flat, gypsum dolomite flat of restricted platform,  
712 dolomite flat, inner shoal and inner mound of open platform, and mound-shoal complex and shoal  
713 of platform margin. The carbonate depositional environment evolved from a shelf (Sq1-Sq2), to a  
714 distal steepening ramp (Sq3-Sq4), to a weekly rimmed platform (Sq5), and finally to a strongly

715 rimmed platform (Sq6-Sq8). A shelf, ramp and rimmed platform carbonate depositional pattern has  
716 been established and six stages of progradational rimmed platform margin deposits composed by  
717 mound-shoal complexes and shoals have been characterized.

718 2. The Lower-Middle Cambrian in the study area can be classified into two 2<sup>nd</sup>-order  
719 stratigraphic sequences (CS1 and CS2) within which eight 3<sup>rd</sup>-order sequences are superimposed.  
720 Within most of the 3<sup>rd</sup>-order sequences, transgressive and regressive system tracts are identified.  
721 Paleo-water depth and relative sea-level changes were reconstructed using microfacies  
722 characteristics and Fischer plots based on the continuous wavelet transform of gamma-ray wireline  
723 logging data, respectively. Paleo-water depth inferred from the microfacies are highly consistent  
724 with the global sea-level change indicated by the carbon isotopes. Reconstructed Paleo-water depth  
725 changes can be divided into eight episodes of rise and fall corresponding to the eight 3<sup>rd</sup>-order  
726 sequences, Sq1-Sq8. A long-term, major maximum flooding surface occurs at the end of the  
727 transgressive system tract of Sq1.

728 3. The existence of favorable prevailing paleocurrents (including paleowinds) and the  
729 development of a slope break zone enabled the development of the carbonate platform in the  
730 northern Tarim Basin during the Cambrian. Evolution of the depositional system was primarily  
731 controlled by tectonics and global sea-level changes. The comparison of paleo-water depth with the  
732 global sea-level change curve demonstrates that the ongoing rate of tectonic subsidence in the study  
733 area during the deposition of the Lower-Middle Cambrian was relatively constant; global sea-level  
734 change was the main factor controlling rimmed platform architecture.

735 4. To date, Ediacrian-Cambrian rimmed carbonate platforms have been poorly documented.  
736 Hence, this study provides valuable information regarding the composition and architecture of a  
737 Cambrian rimmed carbonate platform. As well as documenting the nature of this platform, this study  
738 may act as an analogue to help inform the characteristics of other, less well preserved Ediacrian-  
739 Cambrian rimmed carbonate platforms.

## 740 **Author contribution statement**

741 Author contributions: Qing He: Conceptualization, writing-original draft, writing-review &  
742 editing, methodology, investigation, funding acquisition; Kaibo Shi: writing-review & editing,  
743 validation, resources; Yongsheng Ma, writing-review & editing, validation; Bo Liu: project  
744 administration, writing-review & editing, supervision, resources; Jun Han: writing-review & editing,  
745 resources; Jun Li: data curation; Xiangyu Bai: data curation; Chun Wu: writing-review & editing;  
746 Adam D. McArthur: writing-review & editing, validation; Nigel P. Mountney: writing-review &  
747 editing, validation.

## 748 **Declaration of competing interest**

749 The authors declare that they have no known competing financial interests or personal

750 relationships that could have appeared to influence the work reported in this paper.

## 751 **Acknowledgments**

752 This research was supported by the Science and Technology Major Project of Northwest  
753 Exploration and Production Company of SINOPEC. Number: KY2022-034. Thanks to Associate  
754 Prof. Jinyou He (China University of Geosciences, Beijing) for the discussion on structure and  
755 content of the essay. We would also like to thank Dr. Jinxin Yu (CNOOC) and Dr. Jiangwei Ming  
756 (CNODC) for the discussion on facies analysis. We would like to express our deep thanks and  
757 gratitude to all editorial staff.

## 758 **References**

- 759 Bai, Y., Luo, P., Wang, S., Zhou, C., Zhai, X., Wang, S., Yang, Z., 2017. Structure characteristics and  
760 major controlling factors of platform margin microbial reef reservoirs: A case study of Xiaoerbolak  
761 Formation, Lower Cambrian, Aksu area, Tarim Basin, NW China. *Petrol. Explor. Dev.* 44, 349-358.
- 762 Bai, Y., Xu, A., Liu, W., Zhao, Z., Luo, P., 2019. Sedimentary characteristics of Lower and Middle  
763 Cambrian diamict in the northwestern Tarim Basin. *Nat. Gas. Ind.* 39, 46-57.
- 764 Beauchamp, B., Grasby, S.E., 2012. Permian lysocline shoaling and ocean acidification along NW  
765 Pangea led to carbonate eradication and chert expansion. *Palaeogeogr. Palaeoclimatol. Palaeoecol.*  
766 350, 73-90.
- 767 Bosence, D., Cross, N., Hardy, S., 1998. Architecture and depositional sequences of tertiary fault-block  
768 carbonate platforms; an analysis from outcrop (Miocene, Gulf of Suez) and computer modelling.  
769 *Marine and Petroleum Geology* 15, 203-221.
- 770 Berg, P., Pace, M.L., 2017. Continuous measurement of air-water gas exchange by underwater eddy  
771 covariance. *Biogeosciences* 14, 5595-5606.
- 772 Bosence, D., 2005. A genetic classification of carbonate platforms based on their basinal and tectonic  
773 settings in the Cenozoic. *Sed. Geol.* 175, 49-72.
- 774 Bosence, D.W.J., Wood, J.L., Rose, E.P.F., Qing, H., 2000. Low- and high-frequency sea-level changes  
775 control peritidal carbonate cycles, facies and dolomitization in the Rock of Gibraltar (Early Jurassic,  
776 Iberian Peninsula). *J. Geol. Soc. London.* 157, 61-74.
- 777 Burchette, T.P., Wright, V.P., 1992. Carbonate ramp depositional systems. *Sed. Geol.* 79, 3-57.
- 778 Cao, Y., Li, H., Yan, L., Wang, H., Zhang, J., Yang, M., Zhao, Y., 2018. The sectional evolution  
779 characteristics of Cambrian platform margin in Manxi area of Tarim Basin and its differences in  
780 source-reservoir-cap combination conditions. *Nat. Gas. Geosci.* 29, 796-806.
- 781 Castro, J.M., de Gea, G.A., Ruiz-Ortiz, P.A., Nieto, L.M., 2008. Development of carbonate platforms on  
782 an extensional (rifted) margin: the Valanginian–Albian record of the Prebetic of Alicante (SE Spain).  
783 *Cretac. Res.* 29, 848-860.
- 784 Catuneanu, O., 2019. Model-independent sequence stratigraphy. *Earth-Science Reviews* 188, 312-388.
- 785 Catuneanu, O., Abreu, V., Bhattacharya, J., Blum, M.D., Dalrymple, R.W., Eriksson, P.G., Fielding, C.R.,  
786 Fisher, W.L., Galloway, W.E., Gibling, M.R., Giles, K.A., Holbrook, J., Jordan, R., Kendall,  
787 C.G.S.C., Macurda, B., Martinsen, O.J., Miall, A.D., Neal, J.E., Nummedal, D., Pomar, L.,  
788 Posamentier, H.W., Pratt, B.R., Sarg, J.F., Shanley, K.W., Steel, R.J., Strasser, A., Tucker, M.E.,

789 Winker, C.D., 2009. Towards the standardization of sequence stratigraphy. *Earth-Sci. Rev.* 92, 1-33.  
790 Catuneanu, O., Khalifa, M.A., Wanas, H.A., 2006. Sequence stratigraphy of the Lower Cenomanian  
791 Bahariya Formation, Bahariya Oasis, Western Desert, Egypt. *Sed. Geol.* 190, 121-137.  
792 Chen, D., Tucker, M.E., Zhu, J., Jiang, M., 2001. Carbonate sedimentation in a starved pull-apart basin,  
793 Middle to Late Devonian, southern Guilin, South China. *Basin Res.* 13, 141-167.  
794 Chen, Q., Chu, C., Yang, X., Hu, G., Shi, Z., Jiang, H., Shen, B., Liu, W., 2015a. Sedimentary model and  
795 development of the Cambrian source rocks in the Tarim Basin, NW China. *Petrol. Geol. Exper.* 37,  
796 689-695.  
797 Chen, Q., Yang, X., Chu, C., Hu, G., Shi, Z., Jiang, H., Liu, W., 2015b. Recognition of depositional  
798 environment of Cambrian source rocks in Tarim Basin. *Oil Gas Geol.* 36, 880-887.  
799 Chen, X., Xu, Q., Hao, F., Chen, Y., Yi, Y., Hu, F., Wang, X., Tian, J., Wang, G., 2023. Dolomite reservoir  
800 formation and diagenesis evolution of the Upper Ediacaran Qigebrak Formation in the Tabei  
801 area, Tarim Basin. *Sci. China-Earth Sci.* 66, 2311-2331.  
802 Chen Y, Zhang Y, Wu Y, Zhou P, Li K, Wang X., 2020. Discovery of SPICE and carbon isotope  
803 stratigraphic correlation of the Cambrian Furongian Series in Tarim Craton, NW China. *Science*  
804 *China Earth Sciences*, 63: 1330–1338.  
805 Cloyd, K.C., Demicco, R.V., Spencer, R.J., 1990. Tidal Channel, Levee, and Crevasse-Splay Deposits  
806 from a Cambrian Tidal Channel System: A New Mechanism to Produce Shallowing-Upward  
807 Sequences. *J. Sediment. Petrol.* 60, 73-83.  
808 Colombié, C., Strasser, A., 2005. Facies, cycles, and controls on the evolution of a keep-up carbonate  
809 platform (Kimmeridgian, Swiss Jura). *Sedimentology* 52, 1207-1227.  
810 Daidu, F., Yuan, W., Min, L., 2013. Classifications, sedimentary features and facies associations of tidal  
811 flats. *J. Palaeogeogr.* 2, 66-80.  
812 Diedrich, C., 2002. Vertebrate track bed stratigraphy at new megatrack sites in the Upper Wellenkalk  
813 Member and orbicularis Member (Muschelkalk, Middle Triassic) in carbonate tidal flat  
814 environments of the western Germanic Basin. *Paleogeogr. Paleoclimatol. Paleoecol.* 183, 185-208.  
815 Dunham, R.J., 1962. Classification of carbonate rocks according to depositional textures. In: Ham, W.E.,  
816 (Ed.), *Classification of Carbonate Rocks*. AAPG Memoir, vol. 1, pp. 108–121.  
817 Elrick, M., Read, F.J., 1991. Cyclic ramp-to-basin carbonate deposits, lower Mississippian, Wyoming  
818 and Montana: a combined field and computer modeling study. *J. Sediment. Petrol.* 61 (7), 1194–  
819 1224.  
820 Embry, A.F., 1993. Transgressive–regressive (T–R) sequence analysis of the Jurassic succession of the  
821 Sverdrup Basin, Canadian Arctic Archipelago. *Can. J. Earth Sci.* 30, 301-320.  
822 Feng, Z., Bao, Z., Wu, M., Jin, Z., Shi, X., 2006. Lithofacies palaeogeography of the Cambrian in Tarim  
823 area. *J. Palaeogeogr.* 8, 427-439.  
824 Fischer, A.G., 1964. The Lofer cyclothems of the alpine Triassic. In: Merriam, D.F., (Ed.), *Symposium*  
825 *on Cyclic Sedimentation*. Kansas Geological Survey, Bulletin, vol. 169, pp. 107–148.  
826  
827 Flügel, E., 2010. *Microfacies of Carbonate Rocks, Analysis, Interpretation and Application*. Springer  
828 Berlin, Heidelberg.  
829 Gao, Z., Ding, Q., Hu, X., 2015. Characteristics and controlling factors of carbonate intra-platform shoals  
830 in the Tarim Basin, NW China. *J. Pet. Sci. Eng.* 127, 20-34.  
831 Gao, Z., Fan, T., 2015. Carbonate platform-margin architecture and its influence on Cambrian-  
832 Ordovician reef-shoal development, Tarim Basin, NW China. *Mar. Pet. Geol.* 68, 291-306.

833 Gao, Z., Shi, J., Lv, J., Chang, Z., 2022. High-frequency sequences, geochemical characteristics,  
834 formations, and distribution predictions of the lower Cambrian Yuertusi Formation in the Tarim  
835 Basin. *Mar. Pet. Geol.* 146, 105966.

836 Ge, R., Zhu, W., Wilde, S.A., He, J., Cui, X., Wang, X., Zheng, B., 2014. Neoproterozoic to Paleozoic  
837 long-lived accretionary orogeny in the northern Tarim Craton. *Tectonics*. 33, 302-329.

838 Geyman, E.C., Maloof, A.C., Dyer, B., 2021. How is sea level change encoded in carbonate stratigraphy?  
839 *Earth Planet Sci. Lett.* 560, 116790.

840 Gil, J., Garcia-Hidalgo, J.F., Segura, M., Garcia, A., Carenas, B., 2006. Stratigraphic architecture,  
841 palaeogeography and sea-level changes of a third order depositional sequence: The late Turonian-  
842 early Coniacian in the northern Iberian Ranges and Central System (Spain). *Sed. Geol.* 191, 191-  
843 225.

844 Goldhammer, R.K., Dunn, P.A., Hardie, L.A., 1990. Depositional cycles, composite sea-level changes,  
845 cycle stacking patterns, and the hierarchy of stratigraphic forcing: Examples from Alpine Triassic  
846 platform carbonates. *Geol. Soc. Am. Bull.* 102, 535-562.

847 Goldhammer, R.K., Lehmann, P.J., Dunn, P.A., 1993. The origin of high-frequency platform carbonate  
848 cycles and third-order sequences (Lower Ordovician El Paso Gp, West Texas); constraints from  
849 outcrop data and stratigraphic modeling. *J. Sediment. Res.* 63, 318-359.

850 Graziano, R., 2000. The Aptian–Albian of the Apulia Carbonate Platform (Gargano Promontory,  
851 southern Italy): evidence of palaeoceanographic and tectonic controls on the stratigraphic  
852 architecture of the platform margin. *Cretac. Res.* 21, 107-126.

853 Gu, J., Ma, F., Ji, L., 2009. Types, characteristics and main controlling factors of carbonate platform. *J.*  
854 *Palaeogeogr.* 11, 21-27.

855 Guan, S., Zhang, C., Ren, R., Zhang, S., Wu, L., Wang, L., Ma, P., Han, C., 2019. Early Cambrian  
856 syndepositional structure of the northern Tarim Basin and a discussion of Cambrian subsalt and  
857 deep exploration. *Petrol. Explor. Dev.* 46, 1075-1086.

858 Guo, C., Chen, D., Song, Y., Zhou, X., Ding, Y., Zhang, G., 2018a. Depositional environments and  
859 cyclicity of the Early Ordovician carbonate ramp in the western Tarim Basin (NW China). *J. Asian*  
860 *Earth Sci.* 158, 29-48.

861 Guo, C., Chen, D., Zhou, X., Ding, Y., Wei, W., Zhang, G., 2018b. Depositional facies and cyclic patterns  
862 in a subtidal-dominated ramp during the Early-Middle Ordovician in the western Tarim Basin (NW  
863 China). *Facies* 64.

864 Haq, B.U., Schutter, S.R., 2008. A chronology of Paleozoic sea-level changes. *Science* 322, 64-68.

865 He, B., Jiao, C., Xu, Z., Cai, Z., Zhang, J., Liu, S., Li, H., Chen, W., Yu, Z., 2016. The paleotectonic and  
866 paleogeography reconstructions of the Tarim Basin and its adjacent areas (NW China) during the  
867 late Early and Middle Paleozoic. *Gondwana Research* 30, 191-206.

868 He, F., Lin, C., Liu, J., Zhang, Z., Zhang, J., Yan, B., Qu, T., 2017. Migration of the Cambrian and Middle-  
869 Lower Ordovician carbonate platform margin and its relation to relative sea level changes in  
870 southeastern Tarim Basin. *Oil Gas Geol.* 38, 711-721.

871 Heldt, M., Lehmann, J., Bachmann, M., Negra, H., Kuss, J., 2010. Increased terrigenous influx but no  
872 drowning: palaeoenvironmental evolution of the Tunisian carbonate platform margin during the  
873 Late Aptian. *Sedimentology* 57, 695-719.

874 Herrmann, A.D., Gordon, G.W., Anbar, A.D., 2018. Uranium isotope variations in a dolomitized Jurassic  
875 carbonate platform (Tithonian; Franconian Alb, Southern Germany). *Chem. Geol.* 497, 41-53.

876 Hoffman, P.F., Li, Z.-X., 2009. A palaeogeographic context for Neoproterozoic glaciation. *Palaeogeogr.*



877 Palaeoclimatol. Palaeoecol. 277, 158-172.

878 Hsu, K.J., Siegenth.C, 1969. Preliminary experiments on hydrodynamic movement induced by  
879 evaporation and their bearing on the dolomite problem. *Sedimentology* 12, 11-25.

880 Hu, C., Han, C., Ma, J., Wang, W., Zhao, F., Sun, W., 2023. Reconstruction of paleowind directions  
881 during the Cambrian-Ordovician in the Tarim Basin, Northwestern China. *Palaeogeogr.*  
882 *Palaeoclimatol. Palaeoecol.* 609. 111316.

883 Hu, M., Sun, C., Gao, D., 2019. Characteristics of tectonic-lithofacies paleogeography in the Lower  
884 Cambrian Xiaerbulake Formation, Tarim Basin. *Oil Gas Geol.* 40, 12-23.

885 Hu, X., Fan, T., Gao, Z., Wu, P., 2018. Fischer Plot and Its Response to the Changes of the Early  
886 Ordovician Sea in the Bachu Area, Tarim Basin. *Geol. Sci. Technol. Inf.* 37, 88-95.

887 Huang, B., Xu, B., Zhang, C., Li, Y.a., Zhu, R., 2005. Paleomagnetism of the Baiyisi volcanic rocks (ca.  
888 740Ma) of Tarim, Northwest China: A continental fragment of Neoproterozoic Western Australia?  
889 *Precamb. Res.* 142, 83-92.

890 Huang, S., Tong, H., Liu, L., Hu, Z., Zhang, X., Huan, J., Huang, K., 2009. Petrography, geochemistry  
891 and dolomitization mechanisms of Feixianguan dolomites in Triassic, NE Sichuan, China. *Acta*  
892 *Petrol. Sin.* 25, 2363-2372.

893 Huang, Y., Duan, T., Fan, T., Liu, Y., Shen, L., Zhang, W., Li, M., Zhang, D., 2022. Depositional evolution  
894 history and formation mechanism of Cambrian carbonate platforms in Tahe area: insights from  
895 stratigraphic forward modelling. *Acta Petrol. Sin.* 43, 617-636.

896 Huang, Y., Fan, T., Berra, F., 2020. Architecture and paleogeography of the Early Paleozoic carbonate  
897 systems in the east-central Tarim Basin (China): Constraints from seismic and well data. *Mar. Pet.*  
898 *Geol.* 113, 104147.

899 James, N.P., Vonderborch, C., 1991. Carbonate shelf edge off southern Australia: A prograding open-  
900 platform margin. *Geology* 19, 1005-1008.

901 Jia, C., 1999. Structural characteristic and oil/gas accumulative regularity in Tarim Basin. *Xinjiang Petrol.*  
902 *Geol.* 20, 177-183.

903 Jiang, W., Gao, Z., Hu, Z., Zhao, Y., Chu, C., 2021a. Sedimentary Filling Evolution and Hydrocarbon  
904 Control of High Frequency Sequence in Yurtus Formation, Tarim Basin. *Geoscience* 35, 349-364.

905 Jiang, W., Luo, Q., Shi, K., Liu, B., Wang, Y., Gao, X., 2021b. Origin of a microbial-dominated carbonate  
906 reservoir in the Lower Cambrian Xiaerbulake Formation, Bachu-Tazhong area, Tarim Basin, NW  
907 China. *Mar. Pet. Geol.* 133.

908 Lai, J., Bao, M., Liu, S., Li, D., Wang, S., Yang, K., Chen, X., Wang, G., Ding, X., 2021. Prediction of  
909 high quality deep and ultra-deep dolostones reservoirs in Tarim Basin by well logs. *J. Palaeogeogra.*  
910 23, 1225-1242.

911 Li, J., Jiao, C., Wang, X., Zhang, Z., 2012. The tectonic evolution of Cambrian in Tarim Basin. *Chinese*  
912 *Geol. Sin.* 47, 575-587.

913 Li, Z.-X., Evans, D.A.D., Halverson, G.P., 2013. Neoproterozoic glaciations in a revised global  
914 palaeogeography from the breakup of Rodinia to the assembly of Gondwanaland. *Sed. Geol.* 294,  
915 219-232.

916 Lin, C., Li, S., Liu, J., Qian, Y., Luo, H., Chen, J., Peng, L., Rui, Z., 2011. Tectonic framework and  
917 paleogeographic evolution of the Tarim basin during the Paleozoic major evolutionary stages. *Acta*  
918 *Petrol. Sin.* 27, 210-218.

919 Lin, C., Yang, H., Liu, J., Cai, Z., Peng, I., Yang, X., Yang, Y., 2008. Paleohigh geomorphology and  
920 paleogeographic framework and their controls on the formation and distribution of stratigraphic

921 traps in the Tarim Basin. *Oil Gas Geol.* 29, 189-197.

922 Liu, C., Li, G., Luo, P., Wang, M., Luo, M., Liu, Y., 2016. Seismic Sequences, Evolution and Control  
923 Factors of Large Cambrian Progradational Platform-Slope System in the Northern Tarim Basin,  
924 Northwest China. *Acta Geol. Sin.* 90, 669-687.

925 Liu, Y., Hu, M., Zhang, S., 2022. Types, structural evolution difference and petroleum geological  
926 significance of Cambrian-Ordovician carbonate platforms in Gucheng-Xiaotang area, Tarim Basin,  
927 NW China. *Petrol. Explor. Dev.* 49, 1019-1032.

928 Liu, Z., Deng, K., Shi, Z., Tian, Y., Wang, Y., Shen, F., Tan, Q., Gong, X., 2020. Sedimentary facies and  
929 model of shallow water carbonates platform of the Lower Cambrian Longwangmiao Formation in  
930 Sichuan Basin. *J. Palaeogeogr.* 22, 504-522.

931 Longhitano, S.G., Mellere, D., Steel, R.J., Ainsworth, R.B., 2012. Tidal depositional systems in the rock  
932 record: A review and new insights. *Sed. Geol.* 279, 2-22.

933 Markello, J.R., Koepnick, R.B., Waite, L.E., Collins, J.F., 2008. The Carbonate Analogs Through Time  
934 (Catt) Hypothesis and the Global Atlas of Carbonate Fields—A Systematic and Predictive Look at  
935 Phanerozoic Carbonate Systems, in: Lukasik, J., Simo, J.A. (Eds.), *Controls on Carbonate Platform  
936 and Reef Development*. SEPM Society for Sedimentary Geology, p. 0.

937 Meyers, S.D., Kelly, B.G., O'Brien, J.J., 1993. An Introduction to Wavelet Analysis in Oceanography and  
938 Meteorology: With Application to the Dispersion of Yanai Waves. *Mon. Weather Rev.* 121, 2858-  
939 2866.

940 Michel, J., Borgomano, J., Reijmer, J.J.G., 2018. Heterozoan carbonates: When, where and why? A  
941 synthesis on parameters controlling carbonate production and occurrences. *Earth-Sci. Rev.* 182, 50-  
942 67.

943 Montanez, I.P., Read, J.F., 1992. Eustatic control on early dolomitization of cyclic peritidal carbonates:  
944 Evidence from the Early Ordovician Upper Knox Group, Appalachians. *Geol. Soc. Am. Bull.* 104,  
945 872-886.

946 Naderi-Khujin, M., Tavakoli, V., Seyrafian, A., Vaziri-Moghaddam, H., 2020. How a mud-dominated  
947 ramp changed to a carbonate-clastic oil reservoir: Sea-level fluctuations in cretaceous of the central  
948 Persian Gulf. *Mar. Petrol. Geol.* 116, 104301.

949 Ni, X., Shen, A., Chen, Y., Guan, B., Yu, G., Yan, W., Xiong, R., Li, W., Huang, L., 2015. Cambrian  
950 Carbonate Platform Types, Platform Margin Segmentation Characteristics and Exploration  
951 Enlightenment in Tarim Basin. *Nat. Gas Geosci.* 26, 1245-1255.

952 Noorian, Y., Moussavi-Harami, R., Hollis, C., Reijmer, J.J.G., Mahboubi, A., Omidpour, A., 2022.  
953 Control of climate, sea-level fluctuations and tectonics on the pervasive dolomitization and porosity  
954 evolution of the Oligo-Miocene Asmari Formation (Dezful Embayment, SW Iran). *Sed. Geol.* 427,  
955 106048.

956 Noorian, Y., Moussavi-Harami, R., Reijmer, J.J.G., Mahboubi, A., Kadkhodaie, A., Omidpour, A., 2021.  
957 Paleo-facies distribution and sequence stratigraphic architecture of the Oligo-Miocene Asmari  
958 carbonate platform (southeast Dezful Embayment, Zagros Basin, SW Iran). *Mar. Petrol. Geol.* 128,  
959 105016.

960 Osleger, D., 1991. Subtidal carbonate cycles: implications for allocyclic vs. autocyclic controls. *Geology*  
961 19, 917-920.

962 Osleger, D., Read, J.F., 1991. Relation of eustasy to stacking patterns of meter-scale carbonate cycles,  
963 Late Cambrian, U.S.A. *J. Sed. Petrol.* 61, 1225-1252.

964 Overstreet, R.B., Oboh-Ikuenobe, F.E., Gregg, J.M., 2003. Sequence stratigraphy and depositional facies

965 of Lower Ordovician cyclic carbonate rocks, southern Missouri, USA. *J. Sed. Res.* 73, 421-433.

966 Phelps, R.M., Kerans, C., Loucks, R.G., Da Gama, R.O.B.P., Jeremiah, J., Hull, D., 2014. Oceanographic  
967 and eustatic control of carbonate platform evolution and sequence stratigraphy on the Cretaceous  
968 (Valanginian-Campanian) passive margin, northern Gulf of Mexico. *Sedimentology* 61, 461-496.

969 Pomar, L., 2001. Types of carbonate platforms: a genetic approach. *Basin Res.* 13, 313-334.

970 Pomar, L., Aurell, M., Bádenas, B., Morsilli, M., Al- Awwad, S.F., 2015. Depositional model for a  
971 prograding oolitic wedge, Upper Jurassic, Iberian basin. *Mar. Petrol. Geol.* 67, 556-582.

972 Pomar, L., Brandano, M., Westphal, H., 2004. Environmental factors influencing skeletal grain sediment  
973 associations: a critical review of Miocene examples from the western Mediterranean.  
974 *Sedimentology* 51, 627-651.

975 Pomar, L., Hallock, P., 2008. Carbonate factories: A conundrum in sedimentary geology. *Earth-Sci. Rev.*  
976 87, 134-169.

977 Pomar, L., Haq, B.U., 2016. Decoding depositional sequences in carbonate systems: Concepts vs  
978 experience. *Glob. Planet. Chang.* 146, 190-225.

979 Prokoph, A., Agterberg, F.P., 2000. Wavelet analysis of well-logging data from oil source rock, Egret  
980 Member, offshore eastern Canada. *AAPG Bull.* 84, 1617-1632.

981 Ren, J., Song, J., Liu, S., Zhao, R., Luo, Z., Li, Z., Jin, X., Ma, X., Li, K., Ye, Y., Ding, Y., Li, W., Zhao,  
982 L., Tian, L., 2023. Framework and sedimentary model of microbial mound-bank complex in  
983 Member 2 of Dengying Formation, Sichuan Basin. *Acta Petrol. Sin.* 44, 312-328.

984 Rosenau, N.A., Herrmann, A.D., Leslie, S.A., 2012. Conodont apatite  $\delta^{18}O$  values from a platform  
985 margin setting, Oklahoma, USA: Implications for initiation of Late Ordovician icehouse conditions.  
986 *Paleogeogr. Paleoclimatol. Paleoecol.* 315, 172-180.

987 Sadler, P.M., Osleger, D.A., Montanez, I.P., 1993. On the Labeling, Length, and Objective Basis of  
988 Fischer Plots. *J. Sed. Petrol.* 63, 360-368.

989 Santantonio, M., Scrocca, D., Lipparini, L., 2013. The Ombrina-Rospo Plateau (Apulian Platform):  
990 Evolution of a Carbonate Platform and its Margins during the Jurassic and Cretaceous. *Mar. Petrol.*  
991 *Geol.* 42, 4-29.

992 Schlager, W., 2003. Benthic carbonate factories of the Phanerozoic. *Int. J. Earth Sci.* 92, 445-464.

993 Scholle, P.A., Ulmer-Scholle, D.S., 2003. A color guide to the petrography of carbonate rocks: grains,  
994 textures, porosity, diagenesis, 77. *AAPG Memoir*, pp. 1-486.

995 Scott, R.W., Simo, J.A.T., Scott, R.W., Masse, J.-P., 1993. Cretaceous Carbonate Platform, U.S. Gulf  
996 Coast. In: Simo, T.J.A., Scott, R.W., Masse, J.-P. (Eds.), *Cretaceous Carbonate Platforms*, *AAPG*  
997 *Memoir* 56, pp. 97-109.

998 Servais, T., Cascales-Miñana, B., Harper, D.A.T., Lefebvre, B., Van Bocxlaer, B., Wang, W., 2023.  
999 Cambrian explosion and Ordovician biodiversification or Cambrian biodiversification and  
1000 Ordovician explosion? *Evolving Earth* 1, 100018.

1001 Shang, Y., Gao, Z., Fan, T., Wei, D., Wang, Z., Karubandika, G.M., 2020. The Ediacaran-Cambrian  
1002 boundary in the Tarim Basin, NW China: Geological data anomalies and reservoir implication.  
1003 *Marine and Petroleum Geology* 111, 557-575.

1004 Shembilu, N., Azmy, K., 2021. Carbon-isotope stratigraphy of the Middle-Upper Cambrian in eastern  
1005 Laurentia: Implications for global correlation. *Mar. Petrol. Geol.* 128, 105052.

1006 Shi, K., Liu, B., Jiang, W., Luo, Q., Gao, X., 2018. Nanhua-Sinian tectono-sedimentary framework of  
1007 Tarim Basin, NW China. *Oil Gas Geol.* 39, 862-877.

1008 Song, J., Luo P., Yang S., Zhai X., Zhou G., Lu P., 2012. Carbonate rock microbial construction of the

1009 Lower Cambrian Xiaerblak Formation in Sugaitblak area, Tarim Basin. *J. Palaeogeogr.* 14, 341-  
1010 254.

1011 Stephens, N.P., Sumner, D.Y., 2003. Late devonian carbon isotope stratigraphy and sea level fluctuations,  
1012 Canning Basin, Western Australia. *Paleogeogr. Paleoclimatol. Paleoecol.* 191, 203-219.

1013 Tan, L., Liu, H., Chen, K., Ni, H., Zhou, G., Zhang, X., Yan, W., Zhong, Y., Lyu, W., Tan, X., Zhang, K.,  
1014 2022. Sequence sedimentary evolution and reservoir distribution in the third and fourth members of  
1015 Sinian Dengying Formation, Gaomo area, Sichuan Basin, SW China. *Petrol. Explor. Dev.* 49, 1004-  
1016 1018.

1017 Tissot, B., 1979. Effects on prolific petroleum source rocks and major coal deposits caused by sea-level  
1018 changes. *Nature* 277, 463-465.

1019 Tucker, M.E.W., V. Paul, 1990. *Carbonate Sedimentology*. Blackwell Scientific Publication, Oxford, pp.  
1020 482.

1021 Vail, P.R., 1991. The stratigraphic signatures of tectonics, eustacy and sedimentology - an overview.  
1022 *Cycles and Events in Stratigraphy*, 11(3), 617–659.

1023 Wagner, T., Sinninghe Damsté, J.S., Hofmann, P., Beckmann, B., 2004. Euxinia and primary production  
1024 in Late Cretaceous eastern equatorial Atlantic surface waters fostered orbitally driven formation of  
1025 marine black shales. *Paleoceanography* 19. PA3009.

1026 Wang, E., Li, M., Ma, X., Qian, M., Cao, T., Li, Z., Yang, W., Jin, Z., 2024. Diahopane and diasterane as  
1027 the proxies for paleoenvironment, hydrocarbon generation condition, and shale oil accumulation.  
1028 *Chemical Geology* 670, 122447.

1029 Wang, E., Fu, Y., Guo, T., Li, M., 2025. A new approach for predicting oil mobilities and unveiling their  
1030 controlling factors in a lacustrine shale system: Insights from interpretable machine learning model.  
1031 *Fuel* 379, 132958.

1032 Wang, Q., Liu, J., Lin, C., Li, H., 2022. Depositional evolution, sequence stratigraphic framework and  
1033 its response to relative sea-level change, the Middle and Lower Ordovician carbonate system on  
1034 outcrops, north-western margin of Tarim Basin. *Mar. Petrol. Geol.* 146. 105909.

1035 Wang, X., Li, B., Yang, X., Wen, L., Xu, L., Xie, S., Du, Y., Feng, M., Yang, X., Wang, Y., Pei, S., 2021.  
1036 Characteristics of Guangyuan-Wangcang trough during late Middle Permian and its petroleum  
1037 geological significance in northern Sichuan Basin, SW China. *Petrol. Explor. Dev.* 48, 562-574.

1038 Wei, G., Zhu, Y., Zheng, J., Yu, G., Ni, X., Yan, L., Tian, L., Huang, L., 2021. Tectonic-lithofacies  
1039 paleogeography, large-scale source-reservoir distribution and exploration zones of Cambrian subsalt  
1040 formation, Tarim Basin, NW China. *Petrol. Explor. Dev.* 48, 1114-1126.

1041 Williams, H.D., Burgess, P.M., Wright, V.P., Della Porta, G., Granjeon, D., 2011. Investigating Carbonate  
1042 Platform Types: Multiple Controls and a Continuum of Geometries. *J. Sed. Res.* 81, 18-37.

1043 Wilson, J.L., 1975. *Carbonate Facies in Geologic History*. Springer-Verlag, New York, pp. 1–471.

1044 Wood, R., Liu, A.G., Bowyer, F., Wilby, P.R., Dunn, F.S., Kenchington, C.G., Cuthill, J.F.H., Mitchell,  
1045 E.G., Penny, A., 2019. Integrated records of environmental change and evolution challenge the  
1046 Cambrian Explosion. *Nat. Ecol. Evol.* 3, 528-538.

1047 Wright, V.P., Burgess, P.M., 2005. The carbonate factory continuum, facies mosaics and microfacies: an  
1048 appraisal of some of the key concepts underpinning carbonate sedimentology. *Facies* 51, 17-23.

1049 Xi, S., Xiong, Y., Liu, X., Lei, J., Liu, M., Liu, L., Liu, Y., Wen, H., Tan, X., 2017. Sedimentary  
1050 environment and sea level change of the subsalt interval of Member 5 of Ordovician Majiagou  
1051 Formation in central Ordos Basin. *J. Palaeogeogr.* 19, 773-790.

1052 Xu, Y., Hu, X., Garzanti, E., Sun, G., Jiang, J., Li, J., Zhang, S., Schlagintweit, F., Rao, X., 2023.

1053 Carbonate factories and their critical control on the geometry of carbonate platforms (mid-  
1054 Cretaceous, southern Iran). *Palaeogeography, Palaeoclimatology, Palaeoecology* 625, 111680.

1055 Yan, L., Li, H., Cao, Y., Yang, M., Zhao, Y., 2018. Revolution and segment characteristics of Cambrian  
1056 carbonate platform margin in Manxi area, Tarim Basin. *Nat. Gas. Geosci.* 29, 807-816.

1057 Yang, Z., Luo, P., Liu, B., Liu, C., Ma, J., Chen, F., 2017. The difference and sedimentation of two black  
1058 rock series from Yurtus Formation during the earliest Cambrian in the Aksu area of Tarim Basin,  
1059 Northwest China. *Acta Petrol. Sin.* 33, 1893-1918.

1060 Ye, N., Li, Y., Liu, D., Xie, S., 2014. Sequence Stratigraphy of Cambrian in Tarim Basin. *Xinjiang Geol.*  
1061 32, 487-493.

1062 Yoshida, S., Johnson, H.D., Pye, K., Dixon, R.J., 2004. Transgressive changes from tidal estuarine to  
1063 marine embayment depositional systems: The Lower Cretaceous Woburn Sands of southern  
1064 England and comparison with Holocene analogs. *AAPG Bull.* 88, 1433-1460.

1065 Yu, B., Lin, C., Fan, T., Wang, L., Gao, Z., Zhang, C., 2011. Sedimentary response to geodynamic  
1066 reversion in Tarim Basin during Cambrian and Ordovician and its significance to reservoir  
1067 development. *Earth Sci. Front.* 18, 221-232.

1068 Yu, J., Song, Y., Shi, K., Chen, S., Wang, Q., Liu, B., Han, J., 2022. Depositional facies and sequence  
1069 architecture of the Yijianfang Formation in the Shuntuoguole Low Uplift, Tarim Basin, NW China.  
1070 *Geol. J.* 57, 3135-3157.

1071 Zadeh, P.G., Shafiei, A., 2021. Response of the Pliocene-Pleistocene carbonates to relative sea-level  
1072 changes in Kish Island, Persian Gulf. *J. Afr. Earth Sci.* 183, 104316.

1073 Zhang, J., Hu, M., Feng, Z., Li, Q., He, X., Zhang, B., Yan, B., Wei, G., Zhu, G., Zhang, Y., 2021. Types  
1074 of the Cambrian platform margin mound-shoal complexes and their relationship with  
1075 paleogeomorphology in Gucheng area, Tarim Basin, NW China. *Petrol. Explor. Dev.* 48, 94-105.

1076 Zhang, X., Gao, Z., Maselli, V., Fan, T., 2023. Tectono-sedimentary characteristics and controlling factors  
1077 of the lower-middle Cambrian gypsum-salt rocks in the Tarim Basin, Northwest China. *Mar. Petrol.*  
1078 *Geol.* 151. 106189.

1079 Zhang, Y., Chen, D., Zhou, X., Guo, Z., Wei, W., Mutti, M., 2015. Depositional facies and stratal cyclicity  
1080 of dolomites in the Lower Qiulitag Group (Upper Cambrian) in northwestern Tarim Basin, NW  
1081 China. *Facies* 61, 417.

1082 Zhao, Z., 2015. Indicators of global sea-level change and research methods of marine tectonic sequences:  
1083 take Ordovician of Tarim Basin as an example. *Acta Petrol. Sin.* 36, 262-273.

1084 Zhao, Z., Luo, J., Zhang, Y., Wu, X., Pan, W., 2011. Lithofacies paleogeography of Cambrian sequences  
1085 in the Tarim Basin. *Acta Petrol. Sin.* 32, 938-948.

1086 Zhong, S., Tan, X., Hu, G., Nie, W., Yang, M., Zhang, D., Zheng, J., Xu, J., Dong, G., Xiao, D., Lu, Z.,  
1087 2022. Control of paleogeographic pattern on sedimentary differentiation of evaporite-carbonate  
1088 symbiotic system: A case study of the sixth sub-member of Ordovician Majiagou Formation M5  
1089 Member in central-eastern Ordos Basin, NW China. *Petrol. Explor. Dev.* 49, 837-850.

1090 Zhou, X., Chen, D., Dong, S., Zhang, Y., Guo, Z., Wei, H., Yu, H., 2015. Diagenetic barite deposits in  
1091 the Yurtus Formation in Tarim Basin, NW China: Implications for barium and sulfur cycling in the  
1092 earliest Cambrian. *Precambrian Res.* 263, 79-87.

1093 Zhu, D., Meng, Q., Jin, Z., Liu, Q., Hu, W., 2015. Formation mechanism of deep Cambrian dolomite  
1094 reservoirs in the Tarim basin, northwestern China. *Mar. Petrol. Geol.* 59, 232-244.

1095

1096 Zhu, Y., Ni, X., Liu, L., Qiao, Z., Chen, Y., Zheng, J., 2019. Depositional Differentiation and Reservoir

1097 Potential and Distribution of Ramp Systems during Post-rift Period: An example from the Lower  
1098 Cambrian Xiaoerbulake Formation in the Tarim Basin, NW China. *Acta Sed. Sin.* 37, 1044-1057.  
1099 Zhuravlev, A.Y., Wood, R.A., 2018. The two phases of the Cambrian Explosion. *Sci. Rep.* 8, 16656.  
1100

1101 Fig. 1. Study area is shown. (a) Location of the Tarim Basin in China. (b) Map of the major tectonic  
1102 units and the Middle Cambrian paleogeography of Tarim Basin. Modified from Lin et al. (2011) and  
1103 Wei et al. (2021). The location of the study area is indicated. Note the locations of the studied wells:  
1104 1- Y1, 2- Y2, 3- Y3, 4- Y4, 5- Y5.

1105  
1106 Fig. 2. Seismic profile of Line 1 (shown in Fig. 1b). The division of sequence stratigraphic elements  
1107 of the rimmed carbonate platform margin and the distribution of facies is not clear from seismic  
1108 data before the study.  $T_9^0$ , the bottom of the Lower Cambrian;  $T_8^1$ , the top of the Middle Cambrian;  
1109  $T_8^0$ , the top of the Upper Cambrian.

1110  
1111 Fig. 3. Schematic illustration of the regional Cambrian lithostratigraphic successions and correlation  
1112 between the platform interior zone, the platform margin zone and the basin zone of the Tarim Basin.  
1113 Modified from (Jiang et al., 2021a; Jiang et al., 2021b; Zhao et al., 2011).

1114  
1115 Table 1 Description of microfacies types and microfacies associations of the Middle and Lower  
1116 Cambrian in the Tabei Uplift of Tarim Basin. Abbreviations: A, abundant; F, frequent; C, less  
1117 common; R, rare; N/A, none or absent

1118  
1119 Fig. 4. Photomicrographs of characteristic features of microfacies MF1-MF9b under PPL: (a) PPL  
1120 photomicrographs of Argillite (MF1) in well Y2,  $\in 1y$ , 8647m; (b) PPL photomicrographs of  
1121 Argillaceous limestone (MF2) in well Y1,  $\in 1y$ , 8746m; (c) PPL photomicrographs of Micritic  
1122 limestone (MF3) in well Y4,  $\in 1y$ , 8315m; (d) PPL photomicrographs of Peloid packstone (MF4)  
1123 in well Y1,  $\in 1x$ , 8687m; (e) PPL photomicrographs of Intraclast grainstone (MF5a) in well Y1,  
1124  $\in 1x$ , 8340m; (f) PPL photomicrographs of Rudstone (MF5b) in well Y1,  $\in 1x$ , 8261m; (g) PPL  
1125 photomicrographs of Ooid grainstone (MF5c) in well Y2,  $\in 1x$ , 8230m; (h) PPL photomicrographs  
1126 of Dolomitic limestone (MF6) in well Y1,  $\in 1x$ , 8242.68m; (i) PPL photomicrographs of Calcareous  
1127 dolomite (MF7) in well Y1,  $\in 1x$ , 8431m; (j) PPL photomicrographs of Argillaceous dolomite (MF8)  
1128 in well Y1,  $\in 1w$ , 8130m; (k) Micritic dolomite (MF9a) in well Y4,  $\square 2a$ , 7664m; (l) PPL  
1129 photomicrographs of Finely crystalline dolomite (MF9b) in well Y4,  $\square 2s$ , 7827m.

1130  
1131 Fig. 5. Photomicrographs of characteristic features of microfacies MF9c-MF16 under PPL: (a) PPL  
1132 photomicrographs of Medium-coarse crystalline dolomite (MF9c) in well Y4,  $\square 1w$ , 8094m; (b) PPL  
1133 photomicrographs of Peloid dolo-packstone (MF10) in well Y5,  $\in 2a$ , 8312m; (c) PPL  
1134 photomicrographs of Intraclast dolo wackstone (MF11) in well Y4,  $\square 1w$ , 8039m; (d) PPL  
1135 photomicrographs of Ooid dolo-grainstone (MF12a) in well Y4,  $\square 2s$ , 7738m; (e) PPL

1136 photomicrographs of Intraclast dolo-grainstone (MF12b) in well Y5, □2a, 8227m; (f) PPL  
1137 photomicrographs of Residual intraclast dolomite (MF13) in well Y4, □2a, 7418m; (g) PPL  
1138 photomicrographs of Thrombolite dolomite (MF14a) in well Y5, □2a, 7772m; (h) PPL  
1139 photomicrographs of Strombolite dolomite (MF14b) in well Y4, □2a, 7659m; (i) PPL  
1140 photomicrographs of Foam spongy dolomite (MF14c) in well Y4, □2a, 7578m; (j) PPL  
1141 photomicrographs of Oncoid dolomite (MF14d) in well Y4, □2a, 7640m; (k) PPL  
1142 photomicrographs of Gypsum dolomite (MF15) in well Y1, □2a, 7966m; (l) PPL photomicrographs  
1143 of Anhydrite (MF16) in well Y1, □2a, 7942m.

1144

1145 Fig. 6. Seven microfacies associations (MA1-MA7) inferred to have developed in shelf and ramp  
1146 settings. (a) Variant distribution and relative abundance of microfacies types in different microfacies  
1147 associations are indicated. Facies transition trends and depositional environments are shown; (b-h)  
1148 Main meter-scale depositional cycles developed in different microfacies associations: b- Deep shelf  
1149 (widespread in the Yuertusi Formation), c- Shallow shelf (widespread in the Yuertusi Formation),  
1150 d- Outer ramp (present in well Y4 in the Lower Cambrian), e- Outer middle ramp (widespread in  
1151 the Xiaoerbulake Formation), f- Inner middle ramp (present in well Y1 in the Xiaoerbulake  
1152 Formation), g- Lagoon of middle ramp (present in well Y1 in the Xiaoerbulake Formation), h- Shoal  
1153 of middle ramp (present in well Y2 in the Xiaoerbulake Formation).

1154

1155 Fig. 7. The seven microfacies associations (MA8-MA14) inferred to have developed in carbonate  
1156 platform setting. (a) Variant distribution and relative abundance of microfacies types in different  
1157 microfacies associations are indicated, facies transition trends and depositional environments are  
1158 shown; (b-h) Main meter-scale depositional cycles developed in different microfacies associations:  
1159 b- Muddy dolomite flat (present in well Y1 in the Wusongeer Formation and Middle Cambrian), c-  
1160 dolomite flat (present in well Y3, Y4 and Y5 in the Wusongeer Formation and Middle Cambrian, d-  
1161 gypsum dolomite flat (present in well Y1 and Y2 in the Wusongeer and Awatage formations), e-  
1162 Shoal inner platform (present in well Y4 and Y5 in the Formation), f- Mound inner platform (present  
1163 in well Y4 and Y5 in the Formation), g- Margin mound-shoal complex (present in well Y2, Y3, Y4  
1164 and Y5 in the Wusongeer Formation and Middle Cambrian), h- Margin shoal (present in well Y3, Y4  
1165 and Y5 in the Wusongeer Formation and Middle Cambrian).

1166

1167 Fig. 8. Schematic summary of microfacies, depositional environments, sequence stratigraphic  
1168 framework, Fischer plot, geochemical signatures and relative sea-level change of Lower and Middle  
1169 Cambrian in well Y1. The sampling interval of the cuttings is 2 m. The relative sea-level change  
1170 curve is reconstructed based on microfacies, geochemical characteristics and Fischer plot. RST1,  
1171 regressive systems tract of Sq1; MFS, maximum flooding surface; TST1, transgressive systems tract.

1172

1173 Fig. 9. Schematic summary of microfacies, depositional environments, sequence stratigraphic  
1174 framework, Fischer plot, geochemical signatures and relative sea-level change of Lower and Middle

1175 Cambrian in well Y2. The sampling interval of the cuttings is 5 m. The relative sea-level change  
1176 curve is reconstructed based on microfacies, geochemical characteristics and Fischer plot. RST1,  
1177 regressive systems tract of Sq1; MFS, maximum flooding surface; TST1, transgressive systems tract.  
1178

1179 Fig. 10. Schematic summary of microfacies, depositional environments, sequence stratigraphic  
1180 framework, Fischer plot, geochemical signatures and relative sea-level change of Lower and Middle  
1181 Cambrian in well Y4. The sampling interval of the cuttings is 2 m. The relative sea-level change  
1182 curve is reconstructed based on microfacies, geochemical characteristics and Fischer plot. RST1,  
1183 regressive systems tract of Sq1; MFS, maximum flooding surface; TST1, transgressive systems tract.  
1184

1185 Fig. 11. Seismic facies identified in the present study, and associated interpretations of the  
1186 depositional environment in the Cambrian succession.  
1187

1188 Fig. 12. Interpreted seismic profile of line 2 (see location on Fig. 1b), revealing the pattern of  
1189 Ediacaran rift inside and outside the platform, as well as its control on Cambrian sedimentation.  
1190

1191 Fig. 13. Un-interpreted (a), and interpreted (b, c) seismic profiles of Line 3 in the study area (see  
1192 location on Fig. 1b), showing the geomorphic pattern of the Cambrian platform margin in Lower  
1193 and Middle Cambrian.  
1194

1195 Fig. 14. Correlation of depositional facies within the sequence stratigraphic framework of Lower  
1196 Cambrian in the Tabei Uplift, Tarim Basin, exhibiting the spatiotemporal facies variations within  
1197 third-order depositional sequences.  
1198

1199 Fig. 15. Correlation of depositional facies within the sequence stratigraphic framework of Middle  
1200 Cambrian in the Tabei Uplift, Tarim Basin, exhibiting the spatiotemporal facies variations within  
1201 third-order depositional sequences.  
1202

1203 Fig. 16. Principle and example of Fischer plot. (a) Initial Fischer plot (modified from Fischer (1964)).  
1204 Vertical axis is the accommodation space, and abscissa axis is the time. (b) Improved Fischer plot.  
1205 The vertical axis is the cumulative deviation of average thickness, which means accumulation of D-  
1206 value between each cycle's thickness and the average cycle thickness, abscissa axis is the number  
1207 of cycles (Sadler et al., 1993). (c) Interpretation of Fischer plot in Middle Cambrian, well Y5.  
1208 Fischer plot indicates periodic increases and decreases.  
1209

1210 Table 2 Statistics of high-frequency cycles cycle data of different wells in the Tabei Uplift area in  
1211 the Lower-Middle Cambrian.  
1212

1213 Fig. 17. Correlation of paleo-water depth changes in the Tabei Uplift in the Lower-Middle Cambrian



1214 with the global sea-level curve constructed by (Haq and Schutter, 2008).

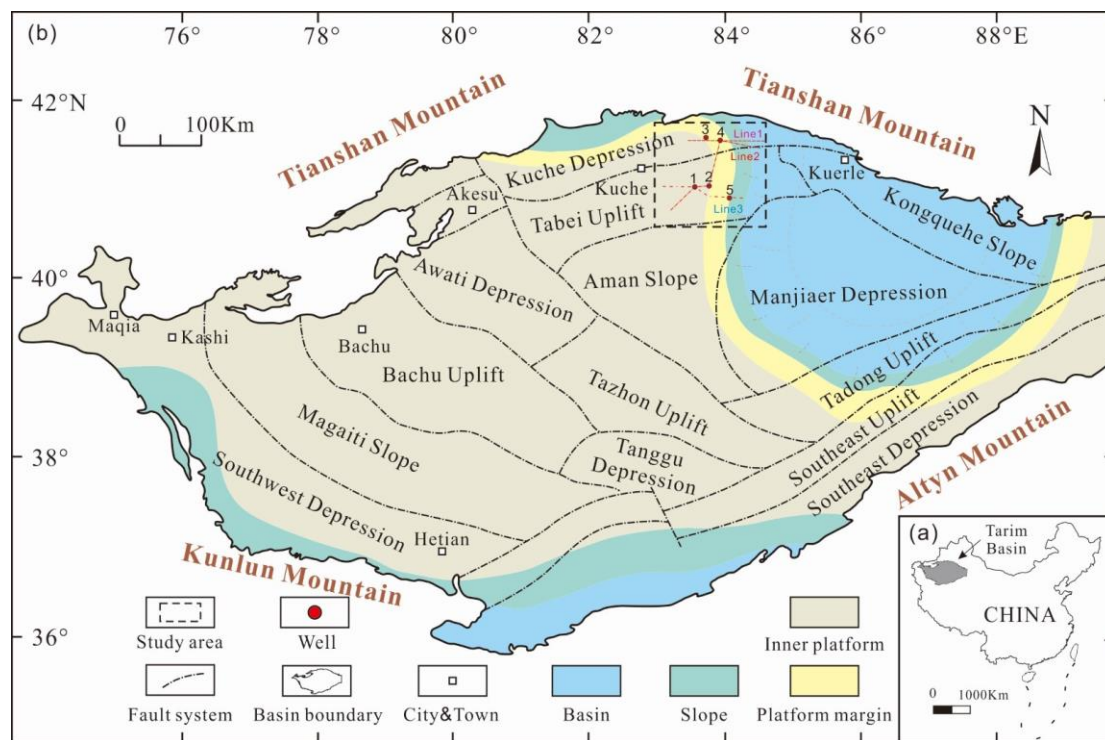
1215

1216 Fig. 18. Depositional evolution pattern of microfacies of the Lower Cambrian platform in the Tabei  
1217 Uplift, Tarim Basin. (a) broad shelf depositional pattern during Sq1-Sq2 period; (b) Distal  
1218 steepening ramp depositional pattern during Sq3-Sq4 period; (c) Distal steepening ramp  
1219 transforming to weakly rimmed platform depositional pattern during Sq5 period. Sq1–Sq5, third-  
1220 order depositional sequence 1–5. RST, regressive systems tract; TST, transgressive systems tract.

1221

1222 Fig. 19. Depositional evolution pattern and the of the Middle Cambrian platform in the Tabei Uplift,  
1223 Tarim Basin. (a) Rimmed Platform depositional pattern during Sq6 (TST6) period; (b) Strongly  
1224 rimmed platform depositional pattern during Sq6 (RST6)-Sq8 period. Sq6–Sq8, third-order  
1225 depositional sequence 6–8. RST, regressive systems tract; TST, transgressive systems tract.

1226

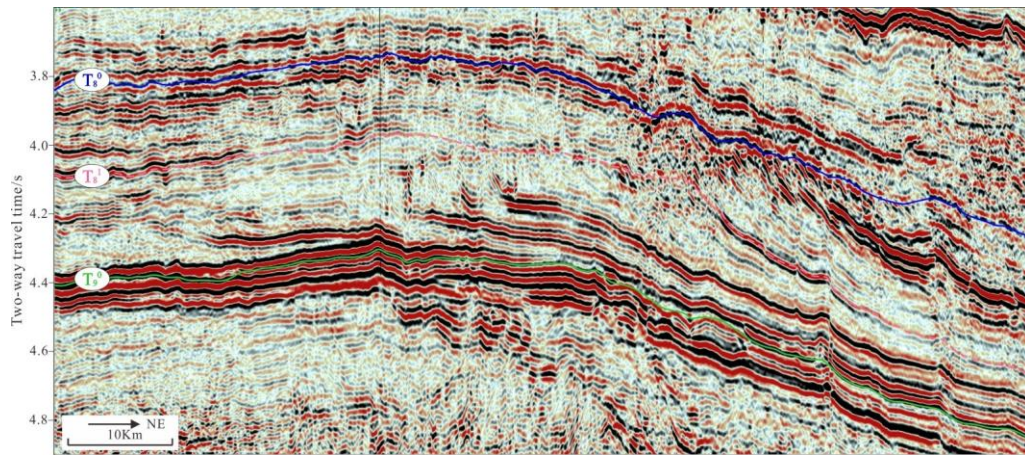


1227

1228

1229 Fig. 1. Study area is shown. (a) Location of the Tarim Basin in China. (b) Map of the major tectonic  
1230 units and the Middle Cambrian paleogeography of Tarim Basin. Modified from Lin et al. (2011)  
1231 and Wei et al. (2021). The location of the study area is indicated. Note the locations of the studied  
1232 wells: 1- Y1, 2- Y2, 3- Y3, 4- Y4, 5- Y5.

1233



1234

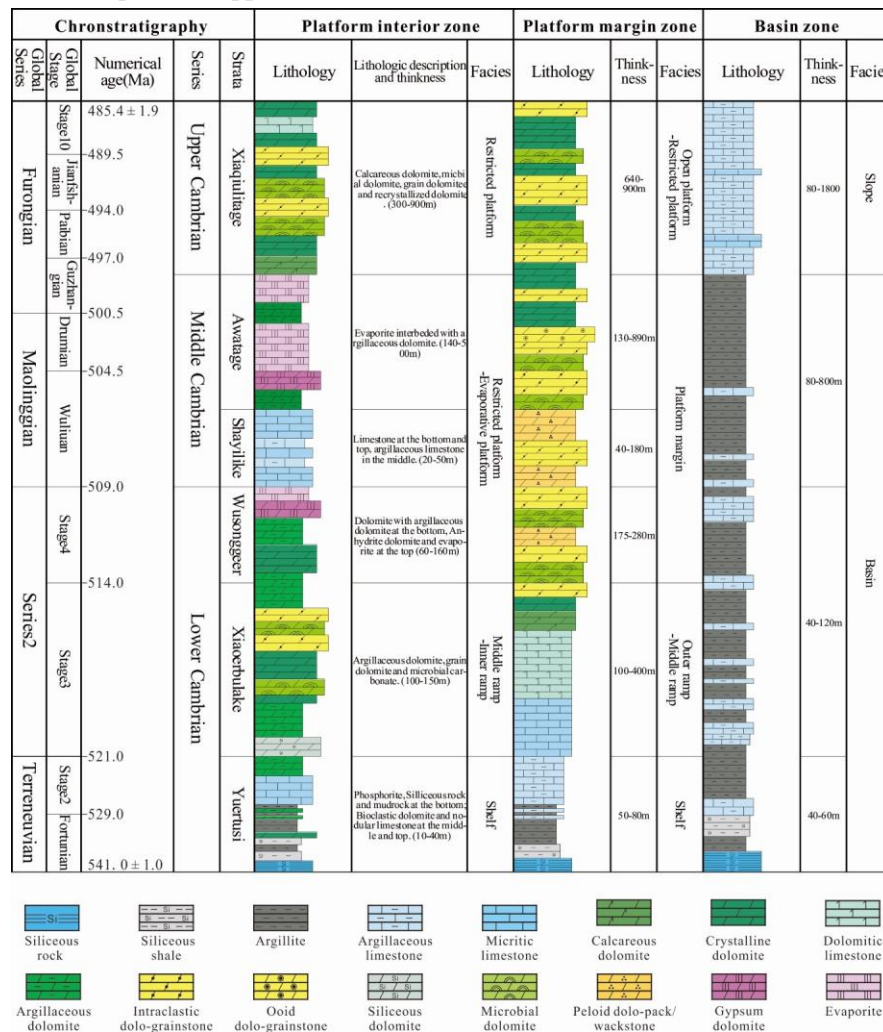
1235

1236

1237

1238

Fig. 2. Seismic profile of Line 1 (shown in Fig. 1b). The division of sequence stratigraphic elements of the rimmed carbonate platform margin and the distribution of facies is not clear from seismic data before the study.  $T_9^0$ , the bottom of the Lower Cambrian;  $T_8^1$ , the top of the Middle Cambrian;  $T_8^0$ , the top of the Upper Cambrian.



1239

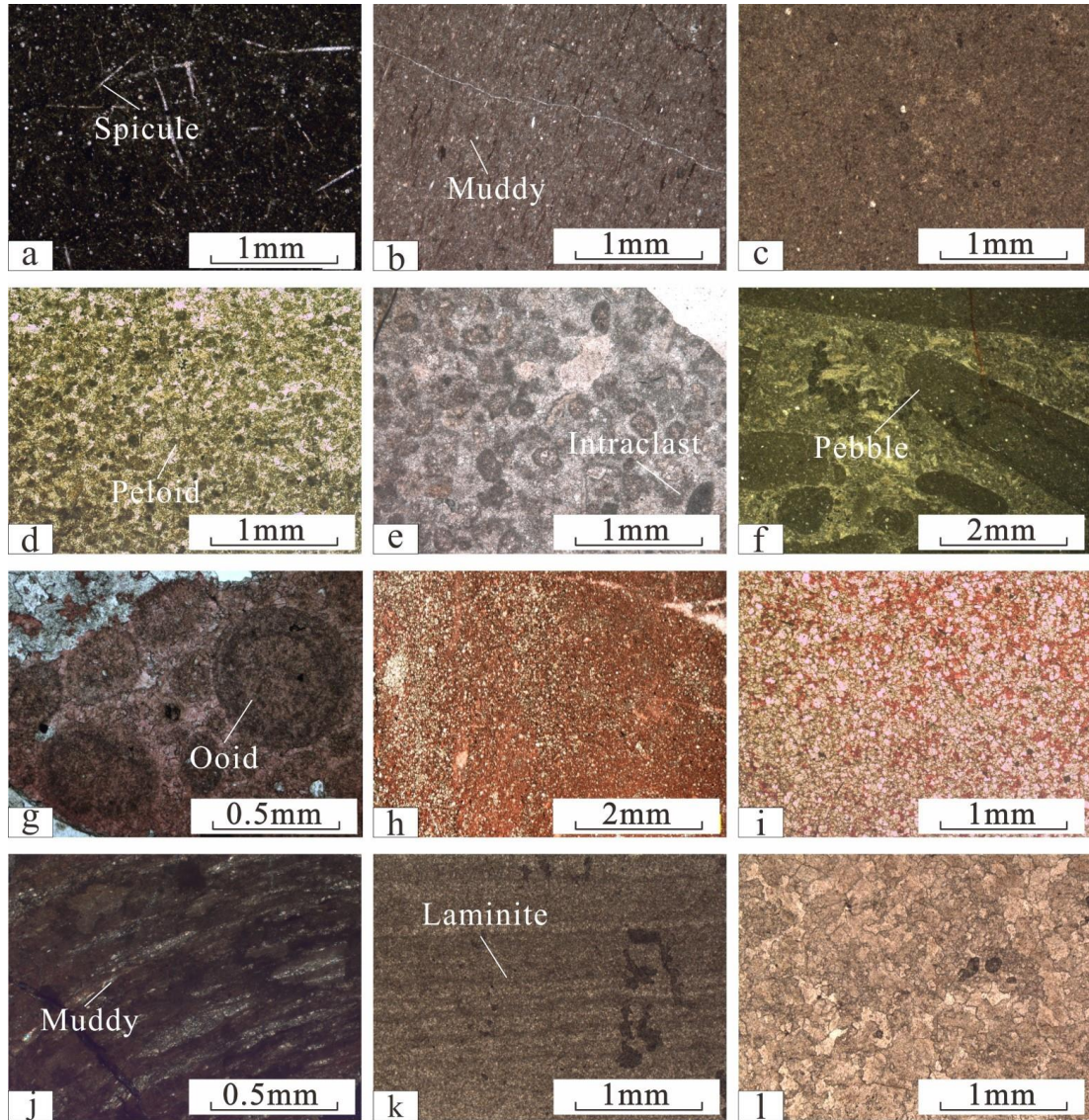
1240

1241

1242

Fig. 3. Schematic illustration of the regional Cambrian lithostratigraphic successions and correlation between the platform interior zone, the platform margin zone and the basin zone of the Tarim Basin. Modified from (Jiang et al., 2021a; Jiang et al., 2021b; Zhao et al., 2011).



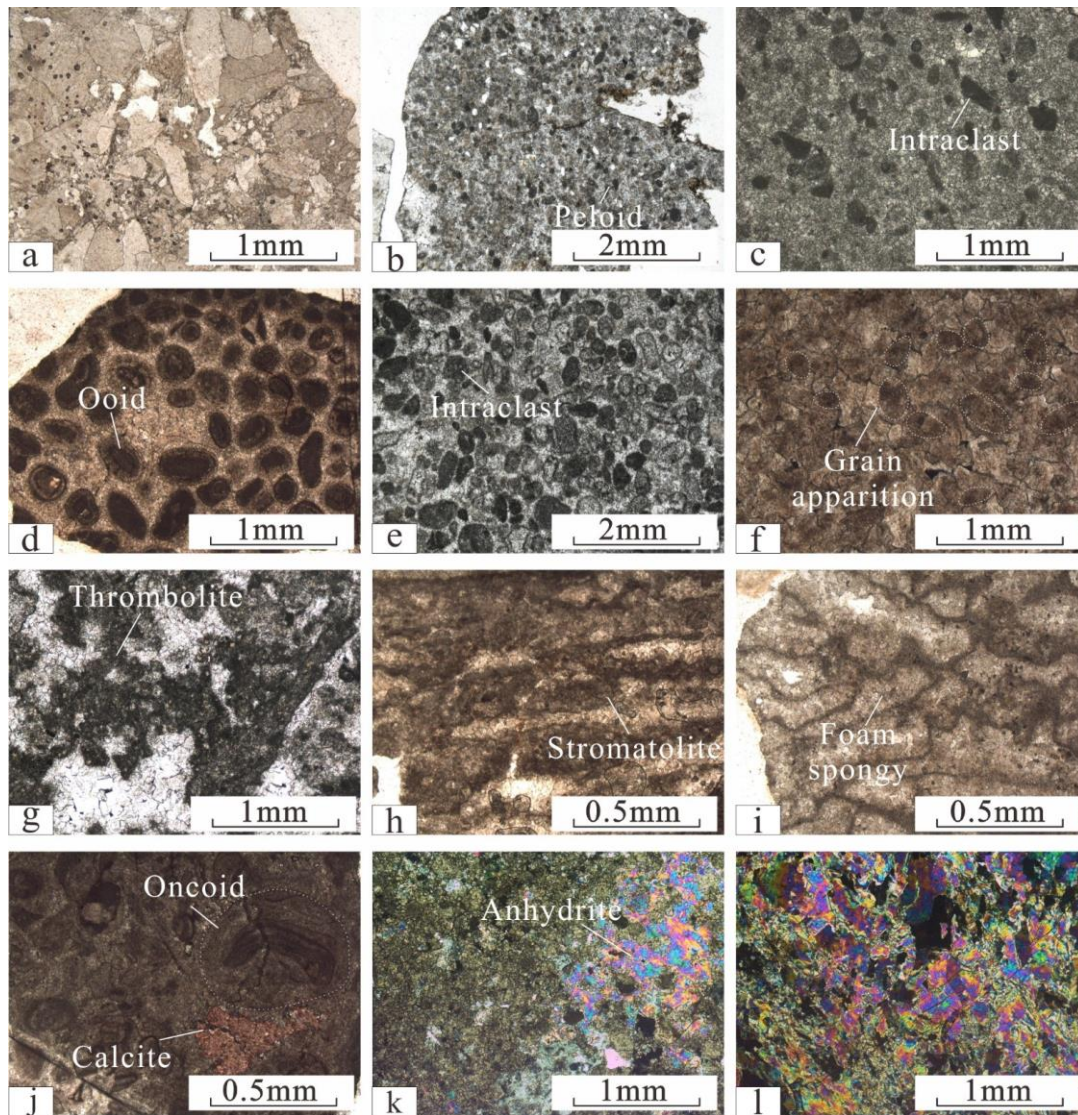


1243

1244

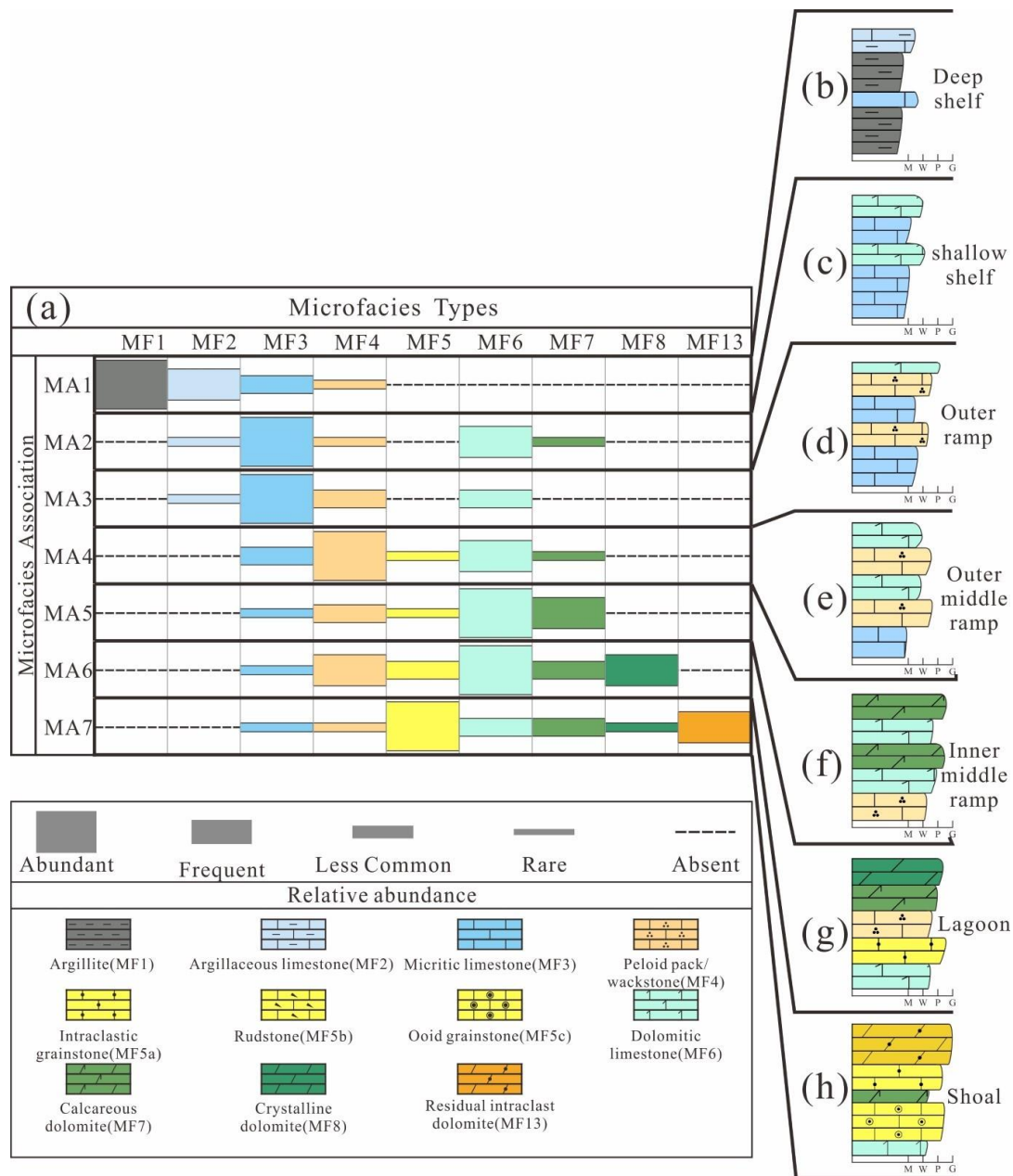
1245 Fig. 4. Photomicrographs of characteristic features of microfacies MF1-MF9b under PPL: (a) PPL  
 1246 photomicrographs of Argillite (MF1) in well Y2,  $\in 1y$ , 8647m; (b) PPL photomicrographs of  
 1247 Argillaceous limestone (MF2) in well Y1,  $\in 1y$ , 8746m; (c) PPL photomicrographs of Micitic  
 1248 limestone (MF3) in well Y4,  $\in 1y$ , 8315m; (d) PPL photomicrographs of Peloid packstone (MF4)  
 1249 in well Y1,  $\in 1x$ , 8687m; (e) PPL photomicrographs of Intraclast grainstone (MF5a) in well Y1,  
 1250  $\in 1x$ , 8340m; (f) PPL photomicrographs of Rudstone (MF5b) in well Y1,  $\in 1x$ , 8261m; (g) PPL  
 1251 photomicrographs of Ooid grainstone (MF5c) in well Y2,  $\in 1x$ , 8230m; (h) PPL photomicrographs  
 1252 of Dolomitic limestone (MF6) in well Y1,  $\in 1x$ , 8242.68m; (i) PPL photomicrographs of  
 1253 Calcareous dolomite (MF7) in well Y1,  $\in 1x$ , 8431m; (j) PPL photomicrographs of Argillaceous  
 1254 dolomite (MF8) in well Y1,  $\in 1w$ , 8130m; (k) Micitic dolomite (MF9a) in well Y4,  $\in 2a$ , 7664m;  
 1255 (l) PPL photomicrographs of Finely crystalline dolomite (MF9b) in well Y4,  $\in 2s$ , 7827m.





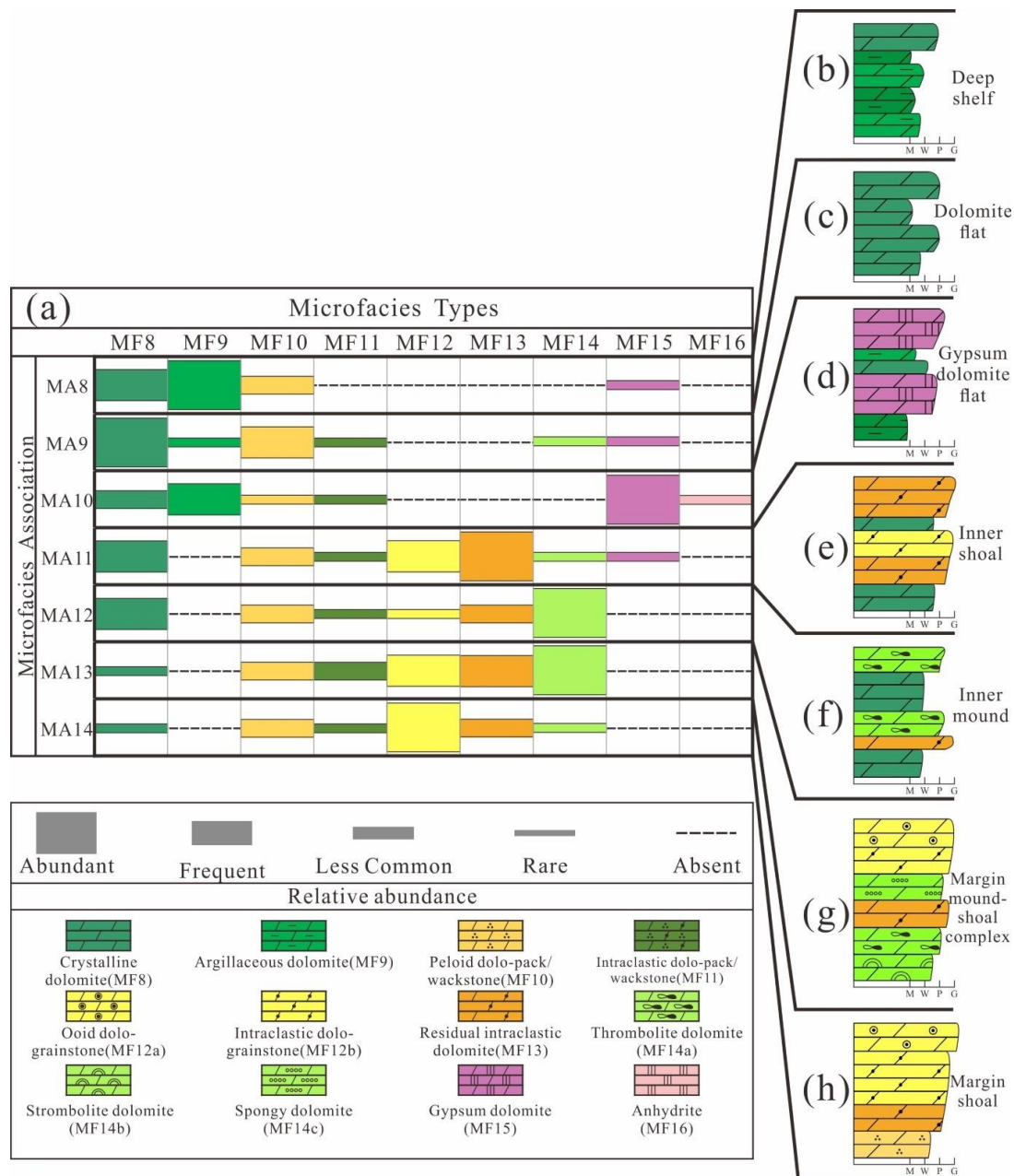
1256  
 1257  
 1258  
 1259  
 1260  
 1261  
 1262  
 1263  
 1264  
 1265  
 1266  
 1267  
 1268  
 1269  
 1270  
 1271

Fig. 5. Photomicrographs of characteristic features of microfacies MF9c-MF16 under PPL: (a) PPL photomicrographs of Medium-coarse crystalline dolomite (MF9c) in well Y4,  $\epsilon$ 1w, 8094m; (b) PPL photomicrographs of Peloid dolo-packstone (MF10) in well Y5,  $\epsilon$  2a, 8312m; (c) PPL photomicrographs of Intraclast dolo wackstone (MF11) in well Y4,  $\epsilon$ 1w, 8039m; (d) PPL photomicrographs of Ooid dolo-grainstone (MF12a) in well Y4,  $\epsilon$ 2s, 7738m; (e) PPL photomicrographs of Intraclast dolo-grainstone (MF12b) in well Y5,  $\epsilon$ 2a, 8227m; (f) PPL photomicrographs of Residual intraclast dolomite (MF13) in well Y4,  $\epsilon$ 2a, 7418m; (g) PPL photomicrographs of Thrombolite dolomite (MF14a) in well Y5,  $\epsilon$ 2a, 7772m; (h) PPL photomicrographs of Strombolite dolomite (MF14b) in well Y4,  $\epsilon$ 2a, 7659m; (i) PPL photomicrographs of Foam spongy dolomite (MF14c) in well Y4,  $\epsilon$ 2a, 7578m; (j) PPL photomicrographs of Oncoid dolomite (MF14d) in well Y4,  $\epsilon$ 2a, 7640m; (k) PPL photomicrographs of Gypsum dolomite (MF15) in well Y1,  $\epsilon$ 2a, 7966m; (l) PPL photomicrographs of Anhydrite (MF16) in well Y1,  $\epsilon$ 2a, 7942m.



1272

1273 Fig. 6. Seven microfacies associations (MA1-MA7) inferred to have developed in shelf and  
 1274 settings. (a) Variant distribution and relative abundance of microfacies types in different microfacies  
 1275 associations are indicated. Facies transition trends and depositional environments are shown; (b-h)  
 1276 Main meter-scale depositional cycles developed in different microfacies associations: b- Deep shelf  
 1277 (widespread in the Yuertusi Formation), c- Shallow shelf (widespread in the Yuertusi Formation),  
 1278 d- Outer ramp (present in well Y4 in the Lower Cambrian), e- Outer middle ramp (widespread in  
 1279 the Xiaerbulake Formation), f- Inner middle ramp (present in well Y1 in the Xiaerbulake  
 1280 Formation), g- Lagoon of middle ramp (present in well Y1 in the Xiaerbulake Formation), h- Shoal  
 1281 of middle ramp (present in well Y2 in the Xiaerbulake Formation).



1282

1283

1284

1285

1286

1287

1288

1289

1290

1291

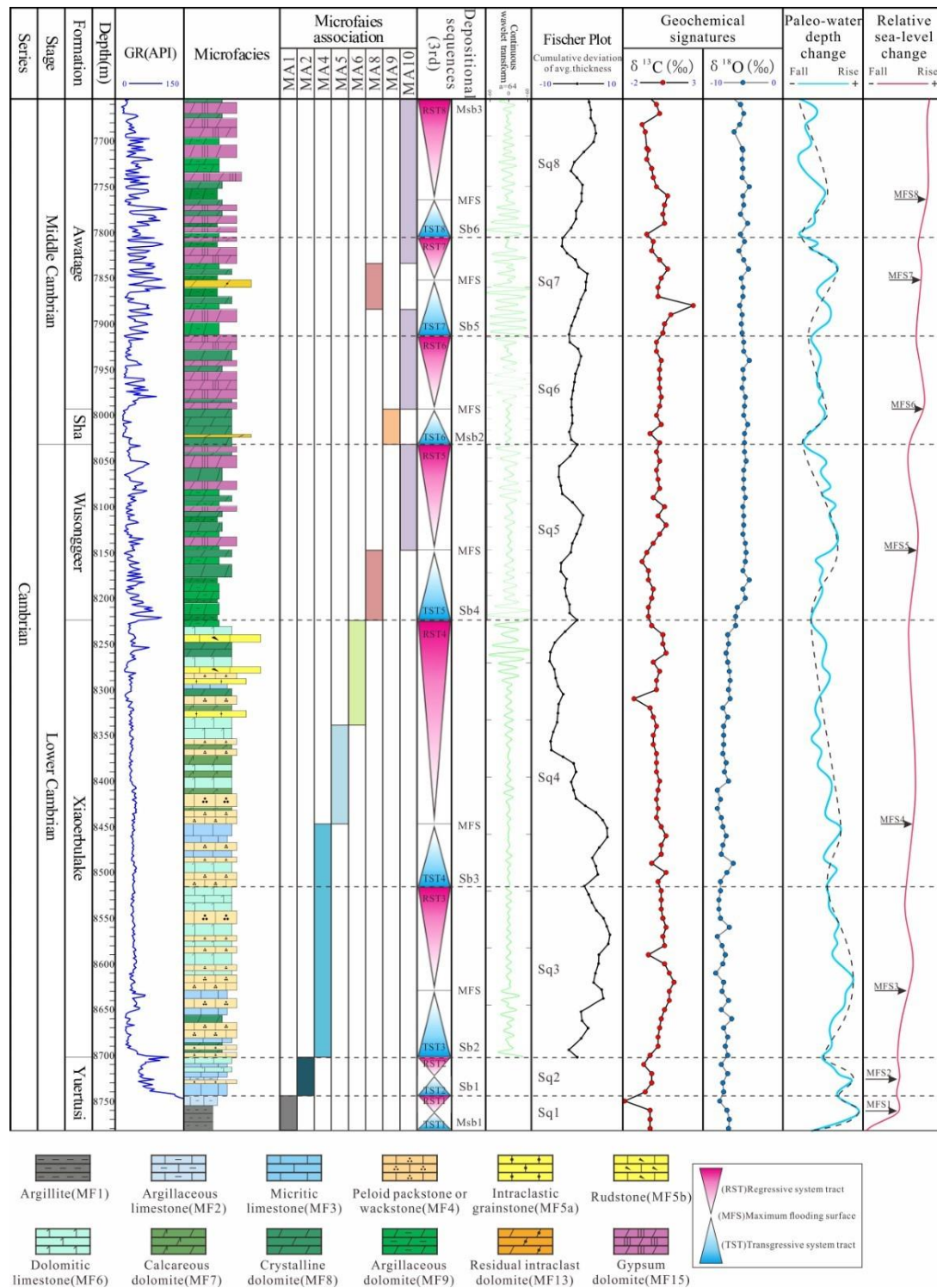
1292

1293

1294

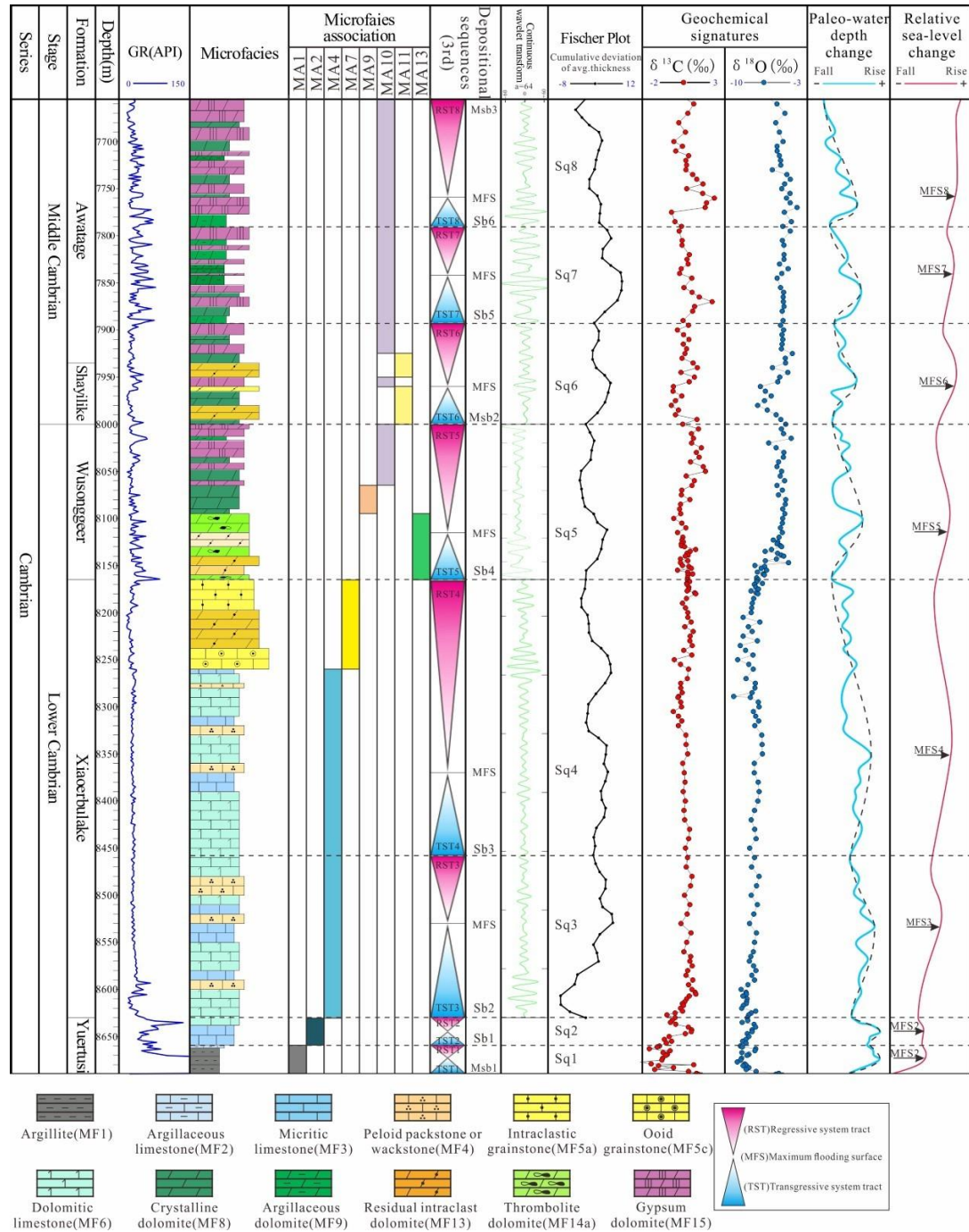
Fig. 7. The seven microfacies associations (MA8-MA14) inferred to have developed in carbonate platform setting. (a) Variant distribution and relative abundance of microfacies types in different microfacies associations are indicated, facies transition trends and depositional environments are shown; (b-h) Main meter-scale depositional cycles developed in different microfacies associations: b- Muddy dolomite flat (present in well Y1 in the Wusongeer Formation and Middle Cambrian), c- dolomite flat (present in well Y3, Y4 and Y5 in the Wusongeer Formation and Middle Cambrian, d- gypsum dolomite flat (present in well Y1 and Y2 in the Wusongeer and Awatage formations), e- Shoal inner platform (present in well Y4 and Y5 in the Formation), f- Mound inner platform (present in well Y4 and Y5 in the Formation), g- Margin mound-shoal complex (present in well Y2, Y3, Y4 and Y5 in the Wusongeer Formation and Middle Cambrian), h- Margin shoal (present in well Y3, Y4 and Y5 in the Wusongeer Formation and Middle Cambrian).





1295  
 1296  
 1297  
 1298  
 1299  
 1300  
 1301  
 1302

Fig. 8. Schematic summary of microfacies, depositional environments, sequence stratigraphic framework, Fischer plot, geochemical signatures and relative sea-level change of Lower and Middle Cambrian in well Y1. The sampling interval of the cuttings is 2 m. The relative sea-level change curve is reconstructed based on microfacies, geochemical characteristics and Fischer plot. RST1, regressive systems tract of Sq1; MFS, maximum flooding surface; TST1, transgressive systems tract.



1303

1304

1305 Fig. 9. Schematic summary of microfacies, depositional environments, sequence stratigraphic  
 1306 framework, Fischer plot, geochemical signatures and relative sea-level change of Lower and Middle  
 1307 Cambrian in well Y2. The sampling interval of the cuttings is 5 m. The relative sea-level change  
 1308 curve is reconstructed based on microfacies, geochemical characteristics and Fischer plot. RST1,  
 1309 regressive systems tract of Sq1; MFS, maximum flooding surface; TST1, transgressive systems  
 1310 tract.



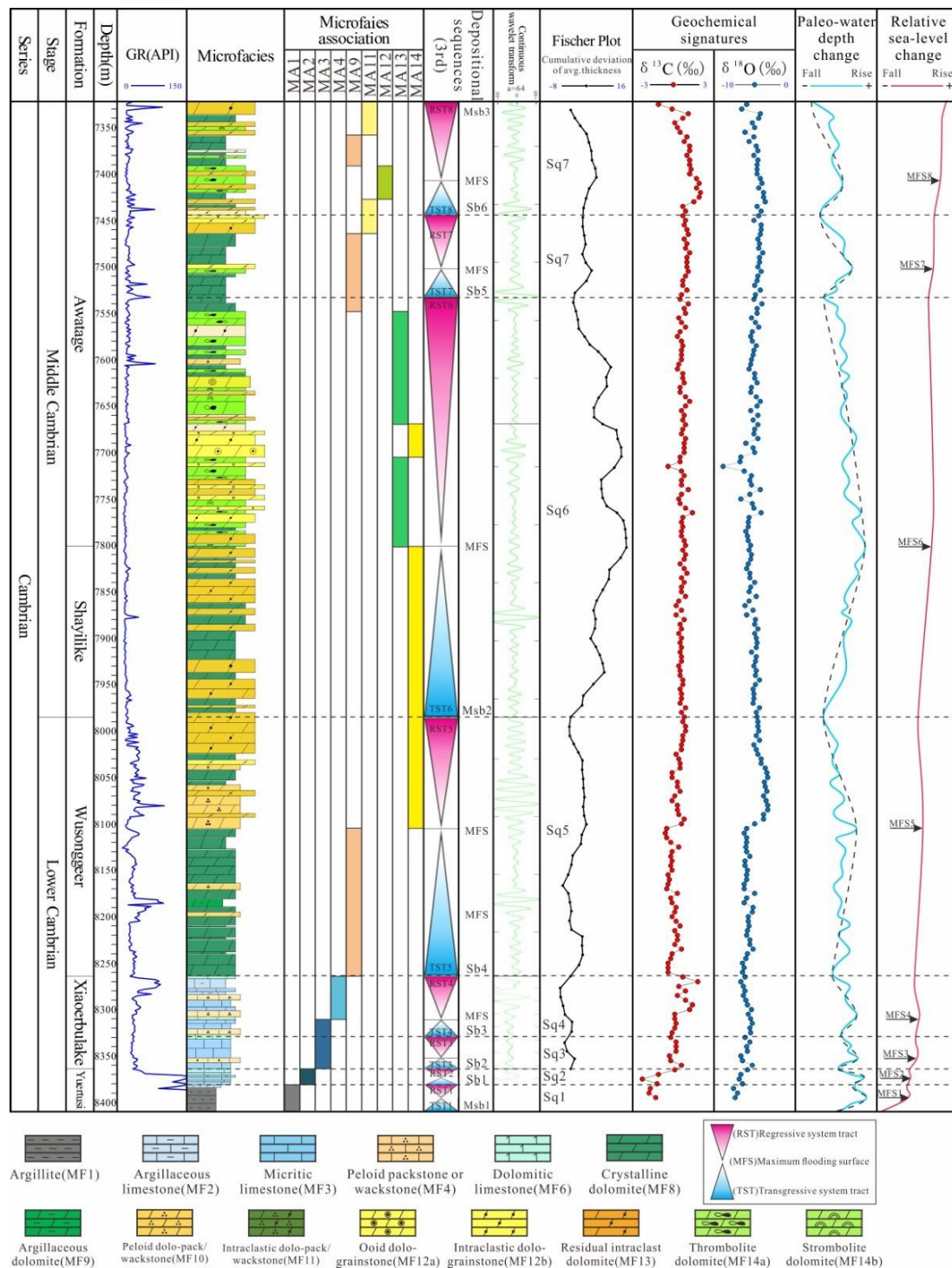
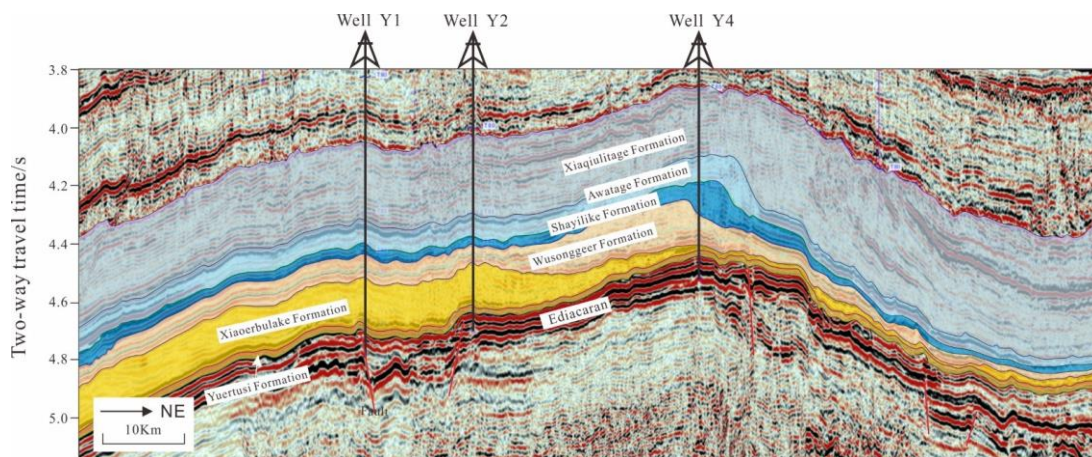


Fig. 10. Schematic summary of microfacies, depositional environments, sequence stratigraphic framework, Fischer plot, geochemical signatures and relative sea-level change of Lower and Middle Cambrian in well Y4. The sampling interval of the cuttings is 2 m. The relative sea-level change curve is reconstructed based on microfacies, geochemical characteristics and Fischer plot. RST1, regressive systems tract of Sq1; MFS, maximum flooding surface; TST1, transgressive systems tract.

Seismic facies type	Seismic proile	Reflection line drawing	Reflection characteristics	Interpretations of environment
SMF1			Sub-parallel reflections Moderate continuous Low-Moderate amplitude Moderate-high frequency	<b>Inner Middle ramp</b>
SMF2			Sub parallel-parallel reflections Moderate-high continuous Moderate-high amplitude Low-moderate frequency	<b>Outer Middle ramp</b>
SMF3			Parallel reflections High continuous High amplitude Low frequency Downlap reflection terminations	<b>Outer ramp-Shelf</b>
SMF4			Sub parallel reflections Moderate-high continuous Moderate-high amplitude Low-moderate frequency	<b>Evaporated tidal flat</b> (Platform interior)
SMF5			Sub parallel-parallel reflections Moderate-high continuous High amplitude Low frequency	<b>Dolomite flat</b> (Platform interior)
SMF6			Sub parallel reflections Moderate continuous Low-moderate amplitude Moderate frequency	<b>Margin shoal</b>
SMF7			Mound and chaotic reflections Low continuous Low-moderate amplitude High frequency	<b>Margin mound-shoal complex</b>
SMF8			Parallel to sub-horizontal reflections High continuous Moderate to high amplitude Low frequency Downlap reflection terminations	<b>Slope</b> (Upper and lower)

1319  
1320  
1321  
1322  
1323

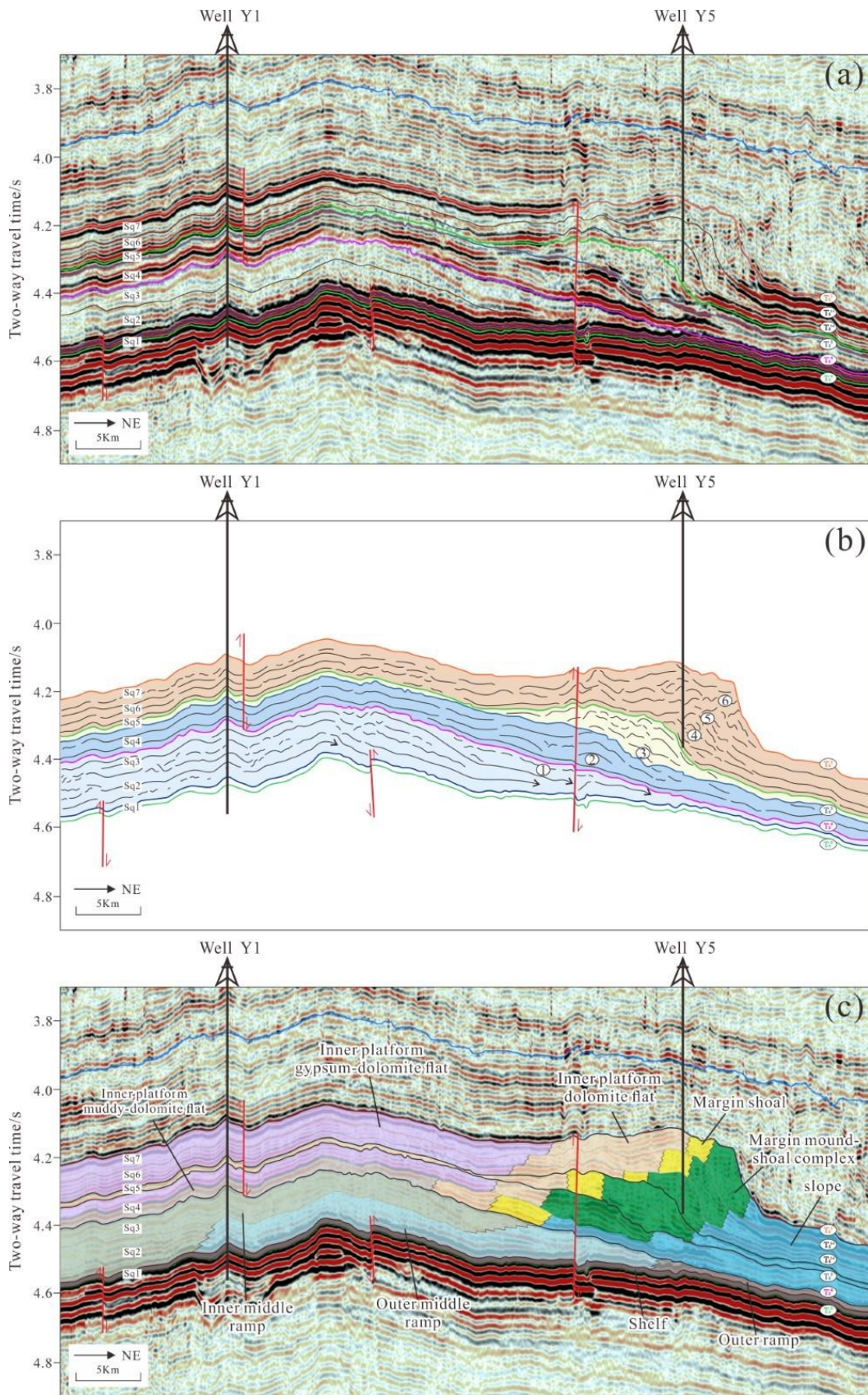
Fig. 11. Seismic facies identified in the present study, and associated interpretations of the depositional environment in the Cambrian succession.



1324  
1325  
1326  
1327

Fig. 12. Interpreted seismic profile of line 2 (see location on Fig. 1b), revealing the pattern of Ediacaran rift inside and outside the platform, as well as its control on Cambrian sedimentation.

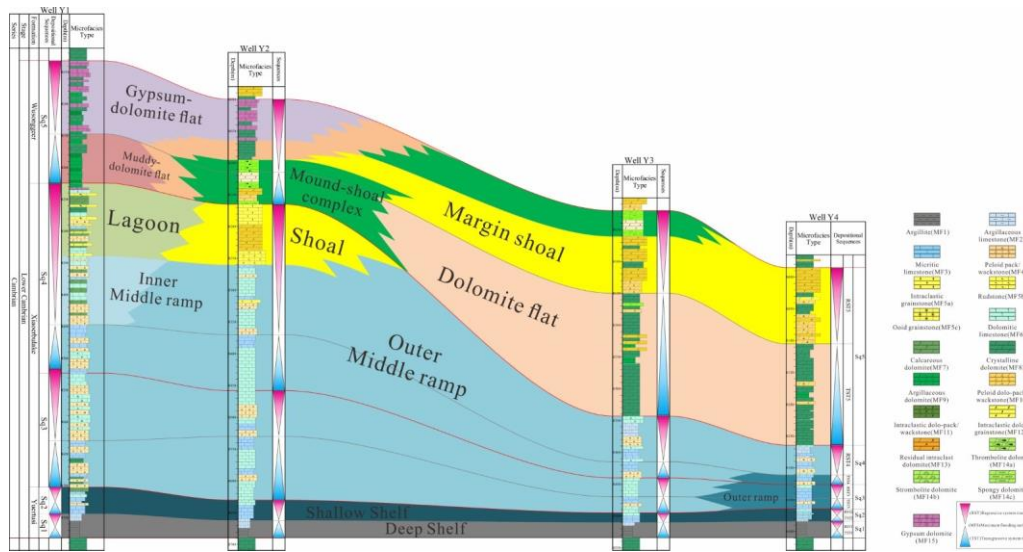




1328

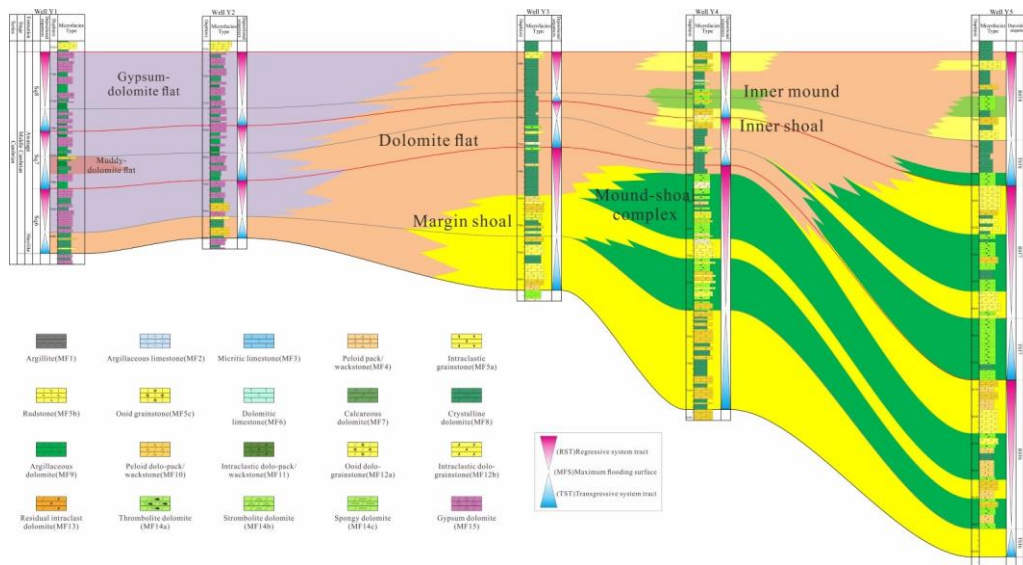
1329 Fig. 13. Un-interpreted (a), and interpreted (b, c) seismic profiles of Line 3 in the study area (see  
 1330 location on Fig. 1b), showing the geomorphic pattern of the Cambrian platform margin in Lower  
 1331 and Middle Cambrian.

1332



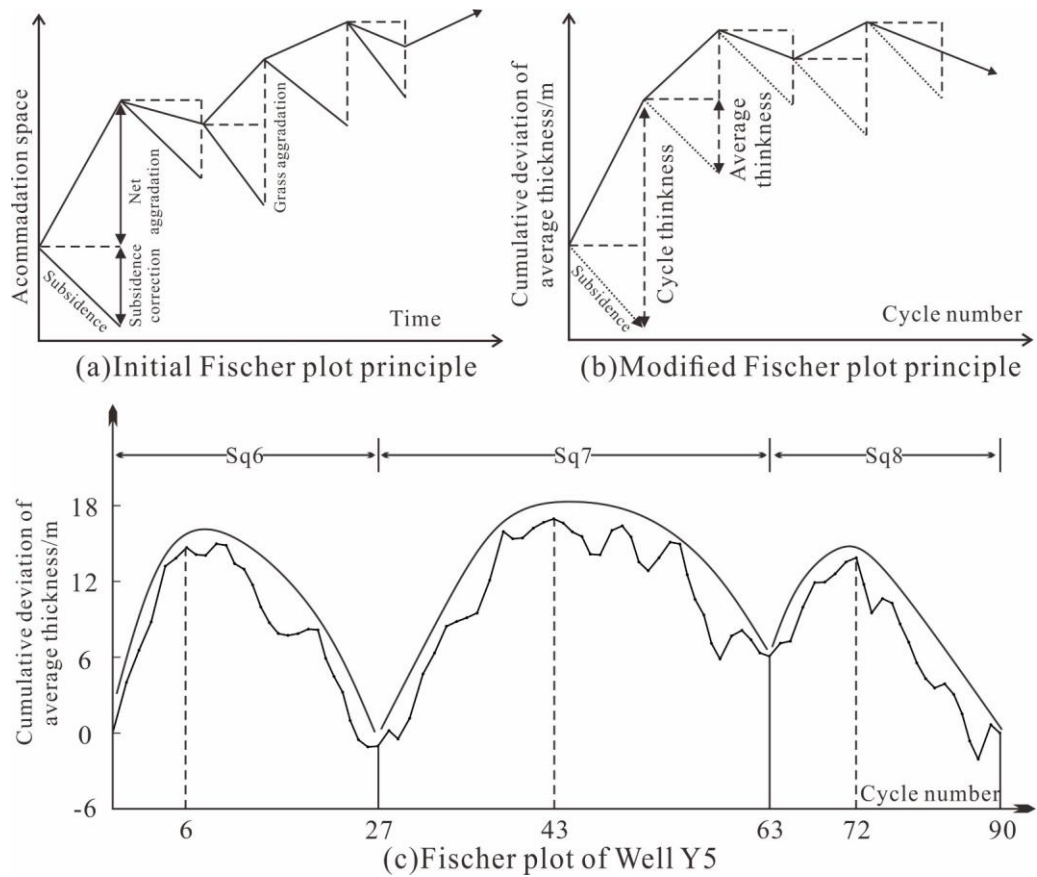
1333

1334 Fig. 14. Correlation of depositional facies within the sequence stratigraphic framework of Lower  
 1335 Cambrian in the Tabei Uplift, Tarim Basin, exhibiting the spatiotemporal facies variations within  
 1336 third-order depositional sequences.



1337

1338 Fig. 15. Correlation of depositional facies within the sequence stratigraphic framework of Middle  
 1339 Cambrian in the Tabei Uplift, Tarim Basin, exhibiting the spatiotemporal facies variations within  
 1340 third-order depositional sequences.  
 1341



1342

1343

1344

1345

1346

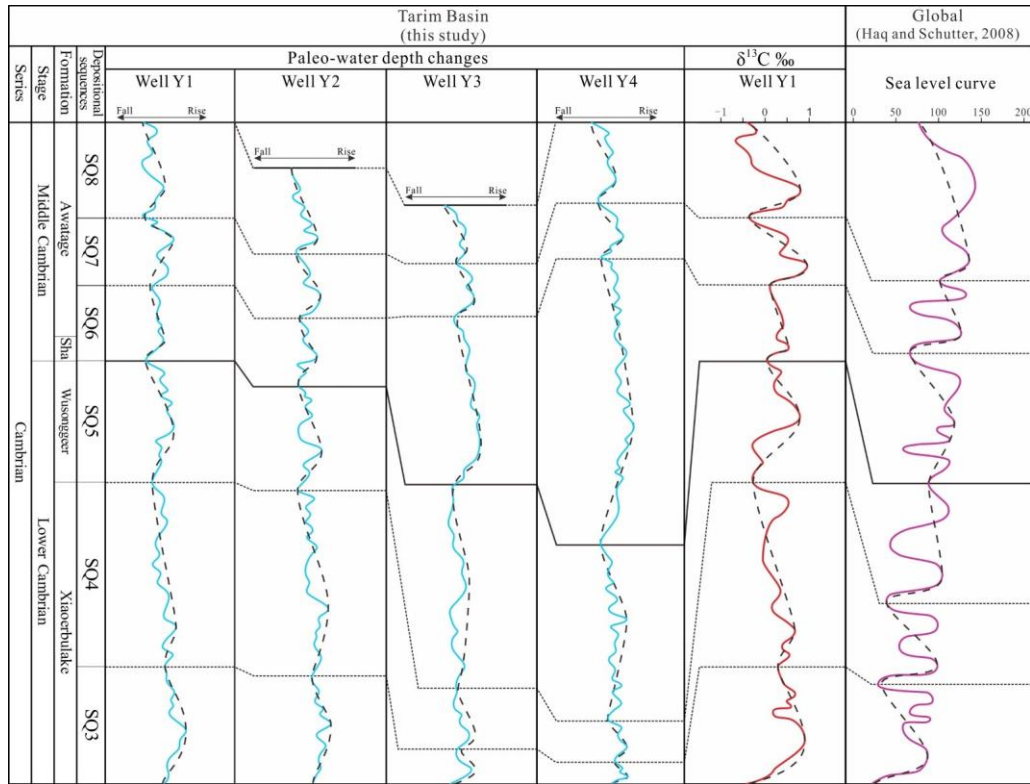
1347

1348

1349

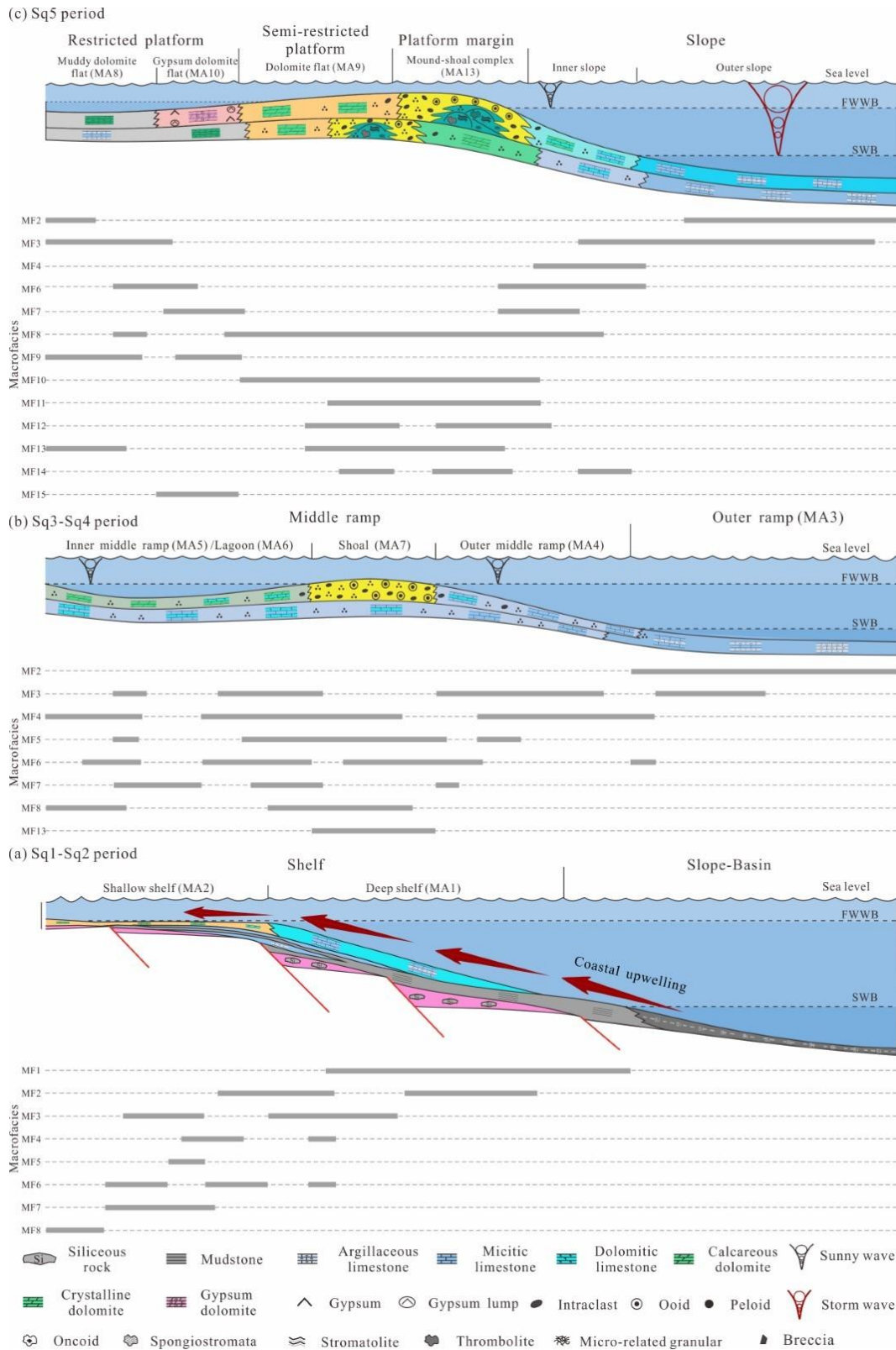
Fig. 16. Principle and example of Fischer plot. (a) Initial Fischer plot (modified from Fischer (1964)). Vertical axis is the accommodation space, and abscissa axis is the time. (b) Improved Fischer plot. The vertical axis is the cumulative deviation of average thickness, which means accumulation of D-value between each cycle's thickness and the average cycle thickness, abscissa axis is the number of cycles (Sadler et al., 1993). (c) Interpretation of Fischer plot in Middle Cambrian, well Y5. Fischer plot indicates periodic increases and decreases.





1350

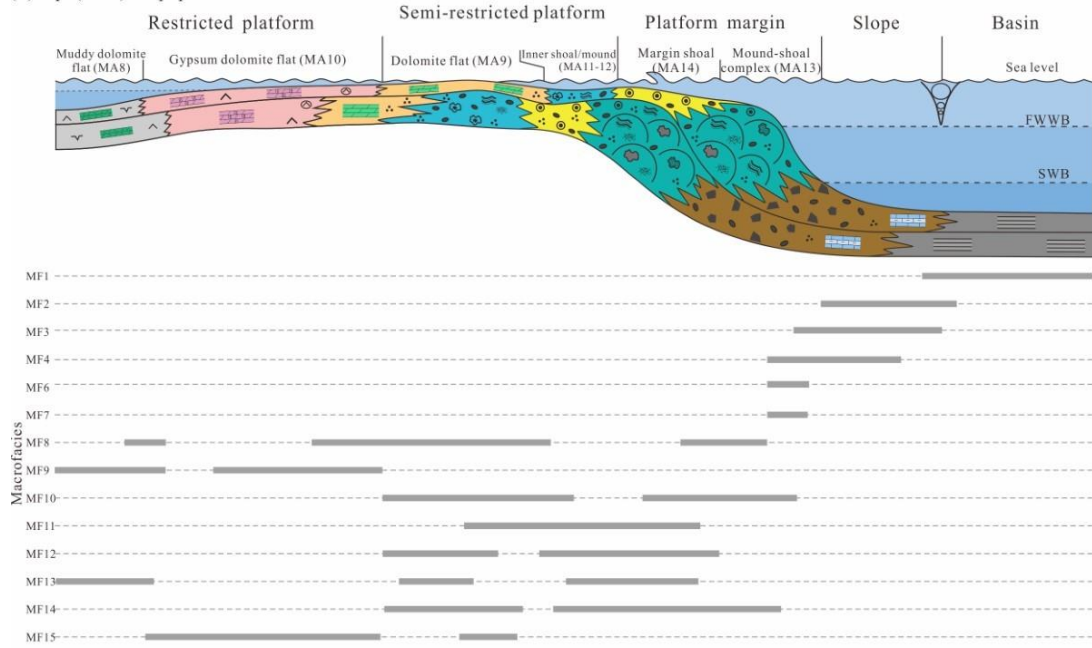
1351 Fig. 17. Correlation of paleo-water depth changes in the Tabei Uplift in the  
 1352 Lower-Middle Cambrian with the global sea-level curve constructed by (Haq and  
 1353 Schutter, 2008).



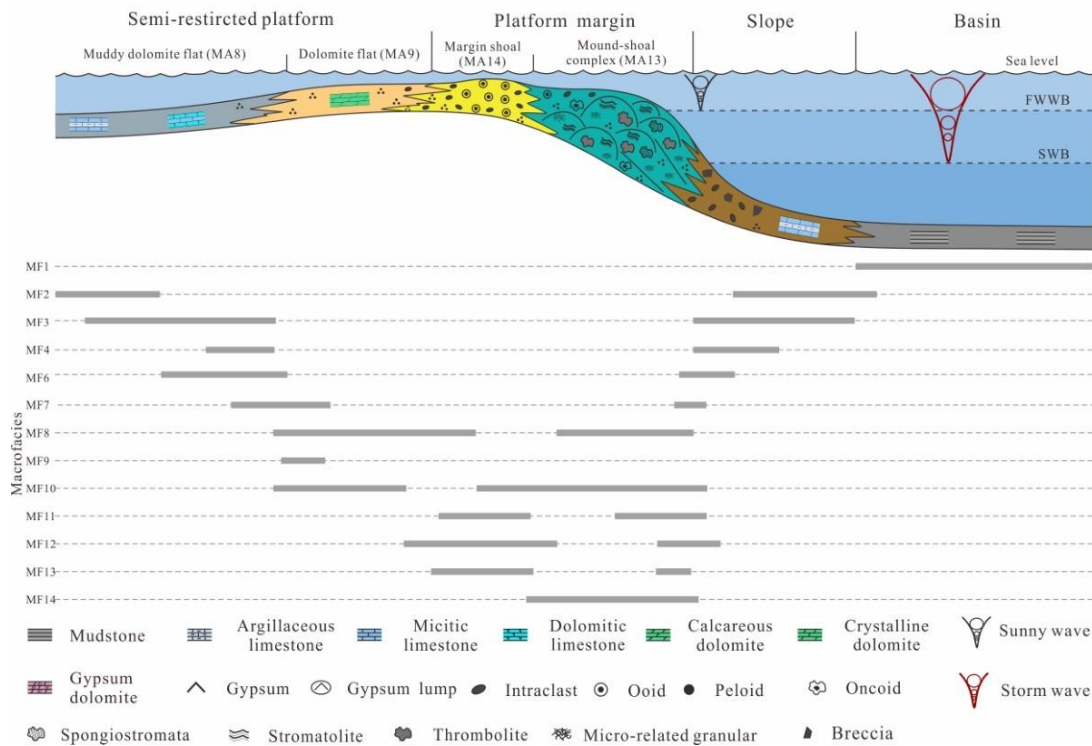
1354

1355 Fig. 18. Depositional evolution pattern of microfacies of the Lower Cambrian platform in the Tabei  
 1356 Uplift, Tarim Basin. (a) broad shelf depositional pattern during Sq1-Sq2 period; (b) Distal  
 1357 steepening ramp depositional pattern during Sq3-Sq4 period; (c) Distal steepening ramp  
 1358 transforming to weakly rimmed platform depositional pattern during Sq5 period. Sq1-Sq5, third-  
 1359 order depositional sequence 1-5. RST, regressive systems tract; TST, transgressive systems tract.

(b) Sq6 (RST) - Sq8 period



(a) Sq6 (TST) period



1360  
1361  
1362  
1363  
1364  
1365  
1366  
1367  
1368  
1369

Fig. 19. Depositional evolution pattern and the of the Middle Cambrian platform in the Tabei Uplift, Tarim Basin. (a) Rimmed Platform depositional pattern during Sq6 (TST6) period; (b) Strongly rimmed platform depositional pattern during Sq6 (RST6)-Sq8 period. Sq6–Sq8, third-order depositional sequence 6–8. RST, regressive systems tract; TST, transgressive systems tract.



1370 Table 1.

Microfacies code	Microfacies name	Description	Composition 1- Non-bioclasts; 2- Bioclasts	Depositional Environment Energy	Relative abundance in different microfacies associations
MF1	Argillite	Black color; high organic matter content; contain much siliceous spicule; widely presents in the study area at the bottom of the Cambrian	1-micrite (R) 2-spicule (A)	Low energy	MA1 (A)
MF2	Argillaceous limestone	Dark grey color; fine laminated texture; composite with some argillaceous material; locally contorted or slump folded (soft sediment deformation structure); rare spicule can be observed; widespends laterally in the study area and overlay by MF1	1- micrite (A) 2-spicule (R)	Low energy	MA1 (F); MA2 (R); MA3 (R)
MF3	Micritic limestone	Light grey to gray color; calcite in composition; exhibited by fine lamination with alternation of mud rich lamina and widespends in the Yuertusi and Xiaoerbulake Formation in the study area	1- micrite (A) 2-peloid (R)	Low energy	MA1 (C); MA2 (A); MA3 (A); MA4 (C); MA5 (R); MA6 (R); MA7 (R)
MF4	Peloid pack/wackstone	Grey to dark grey color; moderately sorted; peloids are very fine–fine (50–100 μm); partial calcite; peloid with a content of 20%-50%; matrix or grain-supported; partial calcite recrystallization; widespends in the Xiaoerbulake Formation in the study area	1-peloid (A); micrite (F) 2-trilobite (C)	Moderate-low energy	MA1 (R); MA2 (R); MA3 (C); MA4 (A); MA5 (C); MA6 (F); MA7 (R)
MF5a	Intraclast grainstone	Grey color; intraclasts are fine–middle (100-500μm) and can be divided into conglomerate, sand and silt size; poorly-moderately sorted; grains are primarily intraclasts a content of 50%-70%; partial calcite recrystallization; grain-supported; only presents on the top of the Xiaoerbulake Formation in well Y1 and Y2	1-intralcast (A); peloid (C) 2-trilobite (R)	High energy	MA4 (R); MA5 (R); MA6 (F); MA7 (F)
MF5b	Rudstone	Light grey to grey color;	1-pebble (A);	High energy	MA5 (R); MA6 (F);

		poorly sorted; grains are primarily pebbleconglomerate-sized intraclasts; coarse (1-2.5mm) grain-supported; intergranular pore spaces cemented by calcite; only presents on the top of the Xiaerbulake Formation in well Y1	peloid (R) 2- trilobite (R)		MA7 (R)
<b>MF5c</b>	Ooid grainstone	Grey color; moderately well sorted; ooids are fine-middle (200-400µm) and can be divided into conglomerate and sand size; contains concentric layer structure; grain-supported and the intergrain is cemented by sparry calcite with fine bright crystalline; only presents on the top of the Xiaerbulake Formation in well Y2	1-oid (A) 2- trilobite (N/A)	High energy	MA6 (C); MA7 (A)
<b>MF6</b>	Dolomitic limestone	Gray color; partial calcite recrystallization; dolomite scattered distribution; calcite with a content of 15%-25%; weak lamination; vugs filled with sparry calcite with fine bright crystalline; widespreads in the Xiaerbulake Formation in the study area	1-micrite (A); peloid (R) 2-Bioclasts (N/A)	Low energy	MA2 (F); MA3 (C); MA4 (F); MA5 (A); MA6 (A); MA7 (C)
<b>MF7</b>	Calcareous dolomite	Dark grey color; calcite undergo dolomitization into very finely crystalline structure; calcite with a content of 25%-50%; vugs filled with sparry calcite with fine bright crystalline; widespreads in the Xiaerbulake Formation in wells Y1, Y2 and Y3	1-very finely crystalline (A); peloid (R) 2-Non	Low energy	MA2 (R); MA4 (R); MA5 (F); MA6 (C); MA7 (C)
<b>MF8a</b>	Micritic-very finely crystalline dolomite	Dark grey; micritic-very fine crystalline structure; rare laminar development with rich muddy; mainly presents in the Wusonggeer and Awatage formations in wells Y1 and Y2	1-micrite-very finely crystalline (A); argillaceous (R) 2- Bioclasts (N/A)	Low energy	MA6 (F); MA7 (R); MA8 (F); MA9 (C); MA10 (C)
<b>MF8b</b>	Finely crystalline dolomite	Grey color; fine crystal structure and the crystals are 100-250µm and without any relict texture; show semi-planar to nonplanar texture; widespreads in the Wusonggeer Formation and	1- finely crystalline (A) 2- Bioclasts (N/A)	Moderate-low energy	MA6 (R); MA8 (R); MA9 (A); MA10 (C); MA11 (F); MA12 (F); MA13 (R); MA14 (R)

		the Middle Cambrian succession in the study area			
<b>MF8c</b>	Middle-coarsely crystalline dolomite	Light gray color; middle-coarse crystal structure, crystals are 250-1000 µm, show planar to semi-planar texture; original component and structure are no longer recognisable without any relict texture; only presents in the Awatage Formation in wells Y4 and Y5	1-middle-coarsely crystalline (A) 2-Non	Moderate energy	MA9 (F) MA11 (C); MA12 (C)
<b>MF9</b>	Argillaceous dolomite	Dark gray to black color; contains argillaceous laminated stripes; slump folded (soft sediment deformation structure); only presents in the Shayilike and Awatage formations in wells Y1 and Y2 and overlay by MF9a	1-micrite (A); argillaceous (F) 2- Bioclasts (N/A)	Low energy	MA8 (A); MA9 (R); MA10 (F)
<b>MF10</b>	Peloid dolo-pack/wackstone	Gery color; moderately-sorted, peloids are very fine-fine (50–100 µm); peloid with a content of 20%-50%; matrix or grain-supported; mainly presents in the Wusonggeer Formation and Middle Cambrian succession in wells Y3, Y4 and Y5	1-peloid (A); micrite (F) 2- Bioclasts (R)	Moderate-low energy	MA8 (C); MA9 (F); MA10 (R); MA11 (F); MA12 (C); MA13 (C); MA14 (C)
<b>MF11</b>	Intraclastic dolo-pack/wackstone	Gery color; the dominant grains are silt-sized (50-200µm) intraclast with a content of 20-40%; The components are minor filaments of bacteria and algae; poorly sorted; matrix or grain-supported; mainly presents in the Middle Cambrian succession in wells Y3, Y4 and Y5	1-intraclast (A); peloid (C) 2-Bioclasts (R)	Moderate energy	MA9 (R); MA10 (R); MA11 (R); MA12 (R); MA13 (C); MA14 (R)
<b>MF12a</b>	Ooid dolo-grainstone	Light grey; ooids are fine-middle (200-500µm) and can be divided into conglomerate and sand size; moderately to well sorted, contains concentric layer structure; grain-supported and the intergrain is cemented by fine crystalline sparry dolomite; mainly presents in the Middle Cambrian succession in wells	1-ooid (A); intraclast (C) 2- Bioclasts (N/A)	High energy	MA11 (R); MA12 (R); MA13 (C); MA14 (C)

		Y4 and Y5			
<b>MF12b</b>	Intraclast dolo-grainstone	Light grey to grey color; intraclasts are fine–middle (200-500µm) and can be divided into conglomerate and sand and silt size; poorly to moderately sorted; grain-supported and the intergrain is cemented by fine crystalline sparry dolomite; mainly presents in the Wusonggeer and the Middle Cambrian succession in wells Y3, Y4 and Y5	1- intraclast (A); peloid (C) 2- Bioclasts (R)	High energy	MA11 (C); MA12 (R); MA13 (C); MA14 (A)
<b>MF13</b>	Residual intraclast dolomite	Light grey color; intraclast is replaced by fine to medium crystalline dolomite with obvious graining lines; the crystalline dolomite is characterized by cloudy at the center and bright around the edges; fine-middle crystal structure; mainly presents in the Wusonggeer and the Middle Cambrian succession in wells Y2, Y3, Y4 and Y5	1-finely-middle crystalline (A); intraclast (R) 2- Bioclasts (R)	Moderate-low energy	MA11 (A); MA12 (C); MA13 (F); MA14 (C)
<b>MF14a</b>	Thrombolite dolomite	Dark grey to grey color; poorly sorted; clotted structure; microbial frameworks are cemented by very fine crystalline sparry dolomite; mainly presents in the Wusonggeer and the Middle Cambrian succession in wells Y2, Y3, Y4 and Y5	1-micrite (F) 2-thrombolite (A)	Moderate-low energy	MA11 (R); MA12 (F); MA13 (A); MA14 (R)
<b>MF14b</b>	Strombolite dolomite	Dark grey to grey color; laminated structure; interactive development of light and dark laminae; develops hummocky or flower - shaped lamina; mainly presents in the Middle Cambrian succession in wells Y3, Y4 and Y5	1-micrite (F) 2-strombolite (A)	Moderate-low energy	MA9 (R); MA11 (R); MA12 (C); MA13 (F);
<b>MF14c</b>	Foam spongy dolomite	Dark grey to grey color; Foam spongy structure; sizes of the spongy frameworks are different and are cemented with sparry dolomite; mainly presents in the Awatage Formation in wells Y4 and Y5	1-micrite (F) 2-spongy (A)	High energy	MA11 (R); MA12 (R); MA13 (C);
<b>MF14d</b>	Oncoidal dolomite	Grey color; oncooids are fine-middle in size (200-500µm);	1-micrite (F); ooid (R)	High energy	MA11 (R); MA12 (R); MA13 (R);

		microbial bonding structure inside oncoids; poorly to moderately sorted; grain-supported with fine crystalline sparry dolomite; mainly presents in the Awatage Formation in wells Y4 and Y5	2-oncoid (A)		MA14 (R)
<b>MF15</b>	Gypsum dolomite	Light grey and grey color; filled with the shape of chicken wire and sausage; dolomite is dominated by micritic crystalline with little content of very fine crystalline dolomite; mainly presents in the Wusonggeer and Awatage formations in wells Y1 and Y2	1-micrite (A); gypsum (C) 2-Bioclasts (N/A)	Low energy	MA8 (R); MA9 (R); MA10 (A); MA11 (R);
<b>MF16</b>	Anhydrite	Brownish grey to brown color; single crystal structure with cluster distribution characteristics; only presents in the Awatage formations in wells Y1 and Y2	1-crystalline gypsum (A) 2-Bioclasts (N/A)	Low energy	MA10 (R)

1371  
1372  
1373  
1374  
1375  
1376  
1377  
1378  
1379  
1380  
1381  
1382  
1383  
1384  
1385  
1386  
1387  
1388  
1389  
1390  
1391  
1392  
1393  
1394  
1395  
1396

1397 Table 2.

Well	Stratigraphy	Total thickness	Cycle number	Average cycle thickness	Max cycle thickness	Min cycle thickness	Microfacies associations
Y1	Sq3-Sq5	670m	69	9.7m	14.6m	6.7m	MA4, MA5, MA6, MA8, MA10
	Sq6-Sq8	378m	47	8.9m	11.3m	7.0m	MA8, MA9, MA10
Y3	Sq3-Sq5	473m	49	9.7m	12.9m	5.8m	MA4, MA9, MA13, MA14
	Sq6-Sq8	442m	47	9.4m	13.0m	6.7m	MA9, MA14
Y2	Sq3-Sq5	630m	67	9.5m	13.9m	6.2m	MA4, MA7, MA9, MA10, MA13
	Sq6-Sq8	345.5m	36	9.8m	13.6m	7.5m	MA10, MA11
Y4	Sq3-Sq5	379m	38	10.0m	12.8m	7.2m	MA3, MA4, MA9, MA14
	Sq6-Sq8	663m	66	9.9m	13.2m	6.5m	MA9, MA11, MA12, MA13, MA14
Y5	Sq6-Sq8	884m	90	9.8m	14.2m	7.4m	MA9, MA11, MA12, MA13, MA14

1398

1399

1400

1401